scientific reports

OPEN

Synthesis and anticancer evaluation of novel thioimidazole derivatives bearing a trimethoxyphenyl moiety

Natalia Maciejewska[1,3]✉, **Birutė Grybaitė**[2,3]✉, **Kazimieras Anusevičius**[2] & **Vytautas Mickevičius**[2]

Nitrogen-containing heterocycles remain central to drug discovery, with imidazole standing out for its versatility and biological relevance. Sulfur substitution yields thioimidazoles, which offer altered electronic properties and pharmacokinetics. In parallel, the 3,4,5-trimethoxyphenyl (TMP) group is recognized as a privileged pharmacophore in oncology, anchoring ligands within protein binding pockets and contributing to multi-target activity. Here, we combined these motifs to synthesize a series of thioimidazole–TMP conjugates. Their activity was tested across human cancer cell models representing distinct tissue origins, alongside non-malignant lung fibroblasts. Among the library, compound 13b emerged as a lead, showing sub-micromolar potency in the most sensitive cancer cells while remaining inactive in fibroblasts, yielding a selectivity index above 20. Mechanistic studies demonstrated that 13b induces a canonical apoptotic program: Annexin V positivity, caspase-3/7 activation, and γH2AX foci consistent with DNA damage. Crucially, these effects extended beyond two-dimensional assays. In three-dimensional spheroid models, which better mimic tumor architecture, 13b penetrated compact structures, suppressed growth, and induced apoptosis in a concentration-dependent manner. Together, these findings indicate that merging thioimidazole and TMP frameworks yields a hybrid scaffold with strong promise in anticancer research. Compound 13b therefore represents a promising candidate for further mechanistic investigation and optimization toward improved drug-like properties.

Keywords Anticancer, Cytotoxicity, Spheroids, Thioimidazole, TMP

Nitrogen-containing heterocyclic scaffolds occupy a central place in modern medicinal chemistry because of their broad biological relevance and therapeutic versatility. Among them, the imidazole ring has received particular attention. As a five-membered aromatic heterocycle with two nitrogen atoms at the 1,3-positions, imidazole exhibits unique tautomeric behavior and remarkable solubility in polar solvents[1]. This simple but versatile motif is naturally embedded in fundamental biomolecules such as histidine, histamine, purines, and nucleic acid bases, underscoring its evolutionary importance in biological recognition and signaling[2].

The distinctive architecture of imidazole allows it to engage enzymes and receptors through hydrogen bonding, π–π stacking, and van der Waals interactions[3]. These features translate into a broad spectrum of biological and pharmacological activities[4–6]. Indeed, imidazole derivatives have been widely explored for their diverse pharmacological properties, including analgesic[7,8], antifungal[9,10], antihypertensive[11,12], anti-obesity[13,14], anticancer[15,16], antiviral[17,18], anthelmintic[19,20], antitubercular[21,22], antiulcer[23,24], anti-inflammatory[25,26], and antidepressant effects[27,28]. Numerous approved drugs carry the imidazole nucleus, including the anticancer mercaptopurine, antifungal azoles such as clotrimazole, ketoconazole, and miconazole, antibiotics of the nitroimidazole class, theophylline (a CNS stimulant), and several antihypertensives and antiprotozoal agents[29]. This track record positions imidazole as a privileged scaffold in drug discovery—modular, versatile, and well suited for further structural innovation in oncology.

[1]Department of Pharmaceutical Technology and Biochemistry, Faculty of Chemistry, Gdansk University of Technology, Narutowicza St 11/12, 80-233 Gdansk, Poland. [2]Department of Organic Chemistry, Kaunas University of Technology, Radvilenu Rd. 19, 50254 Kaunas, Lithuania. [3]Natalia Maciejewska and Birutė Grybaitė have contributed equally to this work. ✉email: natalia.maciejewska@pg.edu.pl; birute.grybaite@ktu.lt

| https://doi.org/10.1038/s41598-026-36890-8

Beyond classical imidazole, sulfur substitution at the heteroaromatic ring has emerged as an attractive structural modification, giving rise to thioimidazole derivatives. The incorporation of sulfur markedly alters the electron distribution and lipophilicity of the core, modifications that frequently translate into enhanced target binding affinity, improved metabolic stability, and potentially favorable pharmacokinetic characteristics[30]. The S-alkylation of thiol (–SH) groups in sulfur-containing compounds represents a key structural modification in synthetic and medicinal chemistry. Alkylation at sulfur converts a thiol into a thioether (R–S–R′) or related S-substituted motif, fundamentally changing the physicochemical properties of the molecule. S-alkylation increases lipophilicity and can alter membrane permeability, metabolic stability, and overall pharmacokinetic profiles compared with the corresponding unalkylated thiol or oxygen analogue. Incorporation of different alkyl substituents at sulfur modulates physicochemical parameters such as lipophilicity, steric bulk, and electronic properties, which in turn affect how compounds interact with biological membranes, metabolizing enzymes, and target proteins. Alkyl groups typically increase non-polar character and membrane permeability, so changing from a small substituent (e.g., methyl) to larger or branched groups (e.g., ethyl, propyl) can meaningfully influence ADME-relevant physicochemical parameters. For example, medicinal chemistry studies show that increasing the length of an S-alkyl chain can correlate with enhanced antimicrobial activity in thioglycoluril derivatives, likely because of greater lipophilicity facilitating cellular uptake, however, the optimal activity is not always monotonic, as steric hindrance and conformational effects also play a role, with some ethyl or propyl derivatives showing reduced potency compared to methyl analogues depending on the scaffold and target[31–35]. Although the body of research on thioimidazoles is still emerging, available studies already indicate their potential in diverse therapeutic areas[36–39]. For instance, compound I has been reported as a cannabinoid CB1/CB2 receptor ligand, while compound II shows notable antitumor effects against carcinomas and lymphosarcoma[40,41] (Fig. 1).

Parallel to imidazole, the 3,4,5-trimethoxyphenyl (TMP) group is now firmly established as a privileged pharmacophore in anticancer medicinal chemistry[42]. This electron-rich aromatic system, with three symmetrically placed methoxy groups, appears in numerous natural and synthetic agents and often determines their biological potency[42]. Its importance was first recognized in natural products such as colchicine and podophyllotoxin, which both target the tubulin cytoskeleton[43,44]. Structural studies revealed that TMP establishes essential hydrophobic and electronic interactions within the colchicine-binding pocket of β-tubulin[45,46]. Importantly, removal or modification of the TMP pattern typically causes a dramatic loss of activity[47]. Synthetic analogues confirmed its indispensability[48]. The combretastatins, in particular combretastatin A-4 (CA-4), demonstrate how TMP anchors ligands within the tubulin site, driving potent antimitotic activity[49]. Owing to its poor aqueous solubility, CA-4 was not pursued as a clinical candidate; instead, its phosphate prodrug fosbretabulin (CA-4P, Zybrestat) was developed to improve formulation properties and subsequently advanced into phase II/III clinical trials as a vascular-disrupting agent[50].

Beyond tubulin, TMP-containing molecules target multiple cancer-relevant pathways[42]. Examples include inhibition of Hsp90[51], thioredoxin reductase[52], lysine-specific demethylase 1 (LSD1)[53], and ALK2[54]. Moreover, TMP fragments have been implicated in overcoming multidrug resistance by modulating P-glycoprotein efflux[55]. This pleiotropy highlights TMP as a genuinely privileged pharmacophore, valued for its ability to confer potency, selectivity, and favorable physicochemical properties[42]. The translational impact of TMP is underscored by clinically approved drugs. Etoposide and teniposide, semisynthetic derivatives of podophyllotoxin, retain the TMP fragment and are widely used topoisomerase II inhibitors in leukemias, lymphomas, and small-cell lung cancer[56–58]. Trimetrexate, an antifolate with oncology applications, also contains a 3,4,5-trimethoxyaniline group critical for DHFR inhibition[59]. These examples demonstrate that TMP is not confined to one mechanism but can be successfully incorporated across diverse anticancer strategies. Taken together, these observations support TMP as a robust cytotoxic pharmacophore suitable for hybridization with heterocyclic scaffolds in anticancer drug discovery.

The convergence of these two privileged motifs—thioimidazole and TMP—represents a rational and literature-supported design strategy. The imidazole nucleus provides chemical tractability and established pharmacological relevance. Sulfur substitution was selected to fine-tune electronic density and lipophilicity, thereby modulating physicochemical properties relevant for small-molecule lead optimization. The TMP group contributes a well-validated pharmacophore crucial for antimitotic activity and multi-target engagement. By combining these frameworks, thioimidazole–TMP conjugates maximize the probability of productive interactions with oncogenic pathways. Literature precedents confirm that TMP-bearing heterocycles outperform their unsubstituted analogues, often inducing apoptosis, DNA damage, and cell cycle arrest[42]. Hybrid molecules uniting TMP with heterocyclic scaffolds such as imidazole, indole, or quinoline have shown robust anticancer activity in glioblastoma, breast, and colon carcinoma models[60–65].

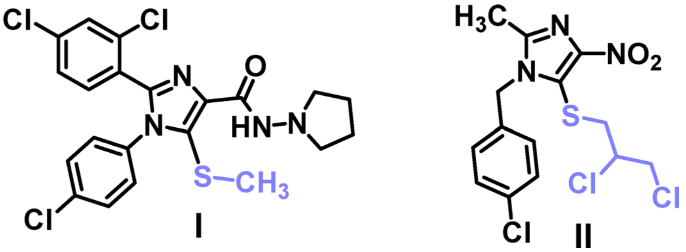

I

II

Fig. 1. Bioactives *S*-alkylated compounds.

Motivated by these compelling pharmacological features, we synthesized novel thioimidazole derivatives incorporating the TMP moiety and investigated their potential anticancer properties.

Results and discussion

Chemistry

In this study, a series of substituted imidazole derivatives bearing a 3,4,5-trimethoxyphenyl moiety were synthesized. Given that many azole-based drugs contain alkoxy moiety and often feature haloaryl rings substituted with fluorine or chlorine atoms, functional groups known to confer favorable physicochemical properties, such as enhanced bioavailability, lipophilicity, and metabolic stability, for this reason 2-bromoacetophenone and 2-bromo-4′-chloroacetophenone were therefore selected as key reagents for the synthesis[66].

The presence of a chlorine substituent in the latter compound enabled the assessment of the influence of a halogen atom on anticancer activity. Initially, 3,4,5-trimethoxyaniline **(1)** reacted with 2-bromoacetophenone or 2-bromo-4′-chloroacetophenone in refluxing methanol for 6 h to give the target aminoketones **2** and **3** (Fig. 2). Analysis of the ^{1}H NMR spectra of the obtained aminoketones reveals an increased intensity of aromatic proton signals (confirmed by ^{1}H NMR, which observes an increase in the signals of aromatic proton atoms), along with a characteristic triplet at 5.62 ppm attributed to the NH group in the compound **2**. In the next stage of the study, the synthetic focus shifted toward the construction of the imidazole core. Aminoketones **2** and **3** served as intermediates and were used to cyclocondensation with potassium thiocyanate in dilute hydrochloric acid. This reaction proceeded smoothly under the applied conditions and led to the formation of 4-(substituted)-1-(3,4,5-trimethoxyphenyl)-1H-imidazole-2-thiol derivatives **4** and **5**. Analysis of the ^{1}H NMR spectra of these compounds reveals the presence of a newly formed SH group of the imidazole ring, observed at 12.96 ppm in the case of compound **4**. These imidazole-2-thiols represent valuable heterocyclic scaffolds with a free thiol group at position 2, offering a handle for further structural modifications. Consequently, compounds **4** and **5** were further alkylated with methyl bromoacetate, yielding the corresponding *S*-alkylated derivatives **6**, **7**.

To synthesized hydrazides **8** and **9**, a nucleophilic substitution reaction of hydrazine monohydrate with the corresponding esters **6** and **7** was carried out. The reaction performed in propan-2-ol under reflux for 5 h afforded 2-((4-(substituted)-1-(3,4,5-trimethoxyphenyl)-1 H-imidazol-2-yl)thio)acetohydrazides **8**, **9**, which were subsequently used for the construction of variously substituted hydrazones and compounds containing the azole cores. Based on hydrazides **8** and **9**, a library of hydrazones **10**–**17** was synthesized (Fig. 3). To achieve this, condensation reactions of compounds **8** and **9** with aromatic aldehydes (for **10a**–**f**, **11a**–**f**, and **14**–**17**) and heterocyclic aldehydes (for **12a**,**b** and **13a**,**b**) were carried out in propan-2-ol. All obtained structures (**10**–**17**) were confirmed by IR, ^{1}H NMR, ^{13}C NMR, and elemental analysis.

Analysis of the ^{1}H NMR spectra of hydrazones **10**–**17** revealed the presence of two characteristic singlets, observed in the ranges of 7.60–8.55 ppm, corresponding to the CH = N group, and 11.32–12.22 ppm, attributed to the NH proton of the hydrazone fragment. The ^{13}C NMR spectra of hydrazones **10**–**17** showed additional resonance signals originating from the carbonyl carbon, azomethine carbon, and newly introduced aryl ring carbons. The complete ^{1}H and ^{13}C NMR spectra are provided in the Supplementary Information (Figs. S17–S56).

To synthesize small molecules relevant for anticancer applications, 3,5-dimethylpyrazole derivatives **18** and **19** as well as 2,5-dimethylpyrrole derivatives **20** and **21** were obtained. The condensation of hydrazides **8** and **9** with the appropriate diketones, as depicted in Fig. 2, was performed in propan-2-ol, with the reactions catalytically accelerated using concentrated hydrochloric acid for compounds **18** and **19**, or glacial acetic acid for compounds **20** and **21**.

In the ^{1}H NMR spectra of pyrazoles **18** and **19**, a characteristic pentet corresponding to the pyrrolic CH proton was observed at 4.91 ppm, while two singlets at 1.17 and 1.19 ppm, integrating for six protons, confirmed the presence of two newly introduced methyl groups, exemplified by compound **18**. Examination of the ^{1}H NMR

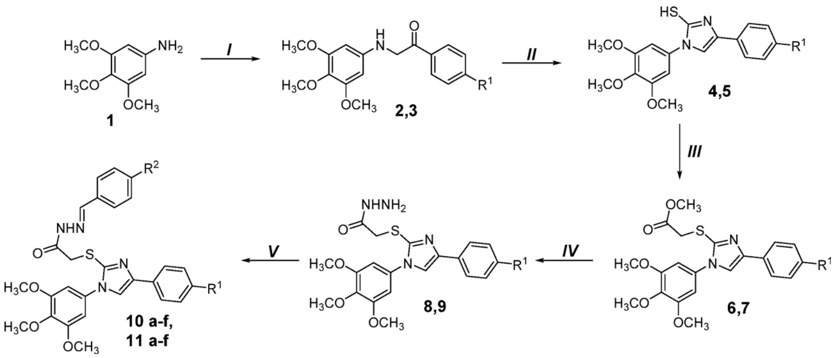

Fig. 2. Synthesis of imidazole derivatives **2 – 11**. **2**, **4**, **6**, **8**, **10** $R^1 = H$; **3**, **5**, **7**, **9**, **11** $R^1 = Cl$; **10a** $R^1, R^2 = H$; **10b** $R^1 = H, R^2 = F$; **10c** $R^1 = H, R^2 = Cl$; **10d** $R^1 = H, R^2 = Br$; **10e** $R^1 = H, R^2 = N(CH_3)_2$; **10f** $R^1 = H, R^2 = NO_2$; **11a** $R^1 = Cl, R^2 = H$; **11b** $R^1 = Cl, R^2 = F$; **11c** $R^1, R^2 = Cl$; **11d** $R^1 = Cl, R^2 = Br$; **11e** $R^1 = Cl, R^2 = N(CH_3)_2$; **11f** $R^1 = Cl, R^2 = NO_2$. **(I)** $C_6H_5COCH_2Br$ or $ClC_6H_4COCH_2Br$, Na_2CO_3, methanol, RT, 5 h; **(II)** KSCN, 10% HCl, reflux, 1 h; **(III)** $BrCH_2COOCH_3$, K_2CO_3, EtOH, reflux, 1h; **(IV)** $N_2H_4{\cdot}H_2O$, i-PrOH, reflux, 5 h; ***(V)*** the corresponding aromatic aldehyde, *i*-PrOH, reflux, 2 h.

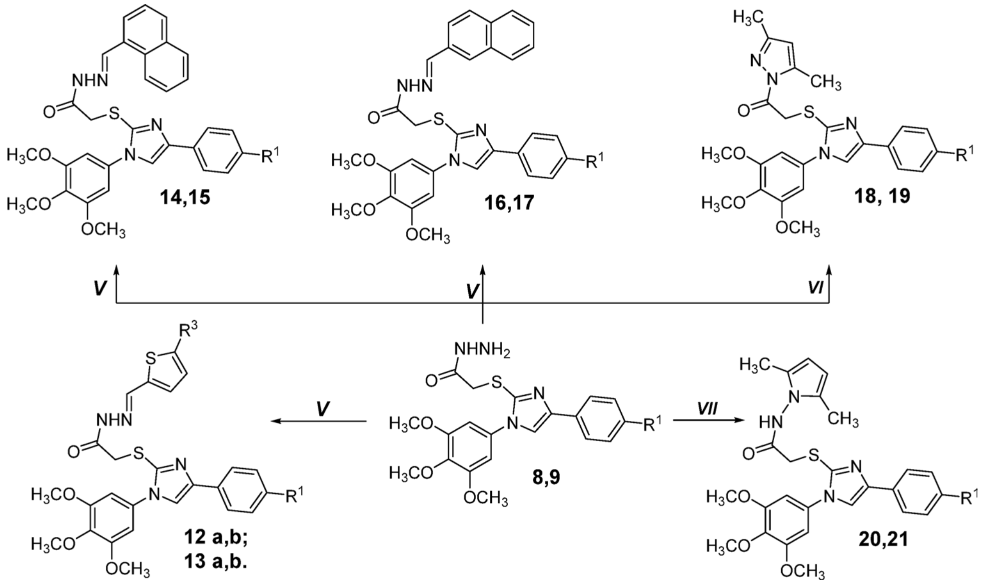

Fig. 3. Synthesis of imidazole derivatives **12 – 21**. **8**, **10**, **12**, **14**, **16**, **18**, **20** $R^1 = H$; **9**, **11**, **13**, **15**, **17**, **19**, **21** $R^1 = Cl$; **12a** R^1, $R^3 = H$; **12b** $R^1 = H$, $R^3 = NO_2$; **13a** $R^1 = Cl$, $R^3 = H$; **13b** $R^1 = Cl$, $R^3 = NO_2$.**V)** the corresponding aromatic aldehyde, i-PrOH, reflux, 2 h; **VI)** pentane-2,4-dione, conc. hydrochloric acid, i-PrOH, reflux, 2 h; **VII)** hexane-2,5-dione, glacial AcOH, i-PrOH, reflux, 3 h.

spectrum of compound **20** revealed an intense singlet at 5.59 ppm, corresponding to the two CH protons of the newly formed pyrrole ring, while two methyl singlets were observed at 1.89 ppm.

Examining the^{1}H NMR spectrum of compound **20**, an intense singlet of the protons of two CH groups of the newly formed pyrrole ring was observed at 5.59 ppm, and singlet of two CH_3 groups were found to resonate at 1.89 ppm. In the^{13}C NMR results, the pyrrole structure was affirmed by the presence of the spectral peaks at 10.97 (2 CH_3), and 102.95 (2 CH), as well as at 126.73 and 126.58 (2 *C*–CH_3) ppm.

Cytotoxic activity of tested compounds across cancer and normal cell lines

The cytotoxic potential of the tested compounds was assessed via the MTT assay after a 72-hour exposure across a panel of four human cancer cell lines—U-2 OS (osteosarcoma), HeLa (cervical carcinoma), HCT-116 (colorectal carcinoma), and A-549 (lung adenocarcinoma)—as well as the non-malignant lung fibroblast line, MRC-5. The corresponding IC_{50} values are presented in Fig. 4; Table 1.

Among the evaluated molecules, several displayed pronounced cytotoxicity, particularly compounds from the 11-series. Compound 11d exhibited IC_{50} values in the range of 5.65–8.31 µM range across all cancer lines, while 11f showed comparable activity (5.25–9.09 µM), suggesting robust antiproliferative efficacy. However, both compounds also demonstrated low IC_{50} values in MRC-5 cells (11.42 ± 2.14 µM and 11.55 ± 0.53 µM, respectively), indicating limited therapeutic selectivity and potential toxicity toward normal cells.

In contrast, compounds **13b**, **17**, **18**, and **21** emerged as highly selective anticancer agents. Notably, **13b** exhibited potent activity in U-2 OS (1.57 ± 0.26 µM), HeLa (2.75 ± 0.07 µM), and HCT-116 (10.63 ± 0.40 µM) cells, while showing no measurable toxicity in MRC-5 (IC_{50} > 100 µM), resulting in a selectivity index (SI) exceeding 20. Similarly, compound **21** maintained IC_{50} values between 8.43 and 16.39 µM across tumor models with no cytotoxicity in MRC-5, highlighting its broad-spectrum activity and favorable safety profile. Compounds **17** and **18** also showed selective cytotoxicity, with moderate-to-strong activity in cancer lines and IC_{50} > 100 µM in normal fibroblasts.

Several compounds, including **10a**, **10b**, **10e**, **12a**, and **19**, demonstrated intermediate cytotoxicity (IC_{50} values typically ranging from 20 to 60 µM) toward specific cancer cell lines while being inactive in MRC-5 cells (IC_{50} > 100 µM). Despite their moderate potency, the absence of toxicity in normal cells suggests these molecules may serve as viable scaffolds for further structure–activity relationship exploration aimed at improving efficacy without compromising safety.

Compounds **10c** and **10d** warrant special attention due to their pronounced cytotoxicity in U-2 OS cells (IC_{50} = 7.58 ± 0.79 µM and 9.04 ± 2.71 µM, respectively), coupled with a complete lack of activity in MRC-5 fibroblasts. However, these compounds exhibited significantly weaker activity in other cancer lines, suggesting a potentially osteosarcoma-selective mechanism. This cell-line-specific response underscores their promise as targeted therapeutic candidates and the necessity for mechanistic studies to elucidate the basis of their selectivity.

Conversely, compounds such as **6**, **7**, **8**, and **9** displayed limited cytotoxicity (IC_{50} > 50 µM across most cancer lines) yet remained non-toxic in MRC-5 cells. While these molecules may currently be considered biologically inert in this model, their structural frameworks could serve as starting points for medicinal chemistry optimization to enhance activity while preserving safety.

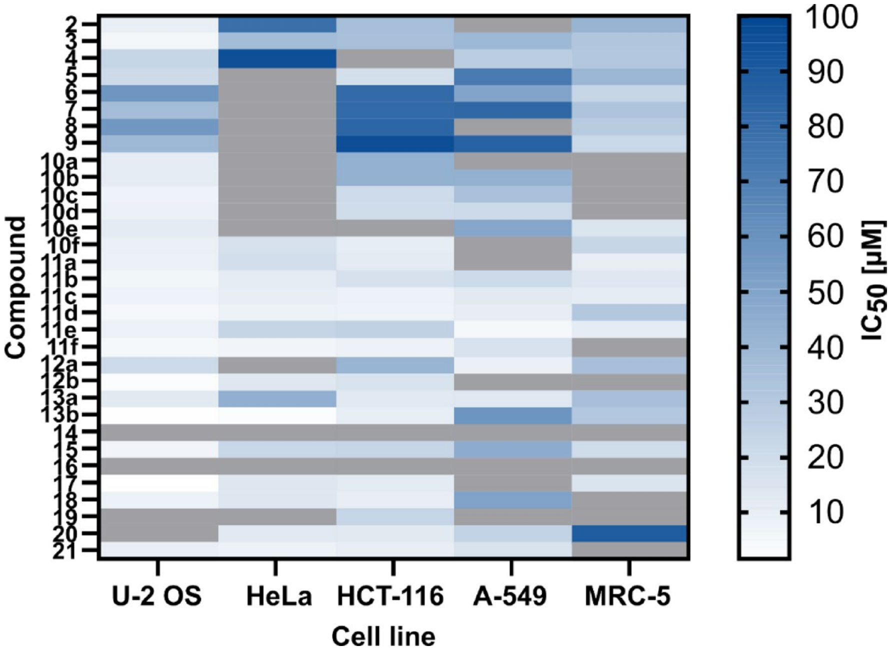

Fig. 4. Heatmap representation of IC_{50} values (μM) for a panel of tested compounds across various cancer and non-cancerous cell lines. Color intensity corresponds to compound potency, with darker shades indicating higher IC_{50} values. Grey boxes denote compounds with no measurable cytotoxic activity within the tested concentration range (IC_{50} > 100 μM). Data are representative of at least three independent experiments.

Finally, compounds **14** and **16** showed no detectable cytotoxicity in any of the tested cell lines (IC_{50} > 100 μM), indicating a lack of anticancer relevance in their current form. Cisplatin, used as a reference compound, exhibited moderate cytotoxicity across all tested cancer cell lines, while showing no measurable toxicity toward normal fibroblasts (MRC-5, IC_{50} > 100 μM). These results are consistent with its known broad-spectrum activity and clinically relevant selectivity profile.

Taken together, the cytotoxicity screening results indicate that compound **13b** is the most promising candidate for more detailed studies, based on its potent antiproliferative activity coupled with an excellent selectivity index (SI > 20). A closer examination of the structure–activity relationships (SAR) within this series provides insight into this superior performance. In general, introducing a chlorine substituent on the phenylacetyl moiety of the imidazole (R_1 = Cl) often enhanced anticancer potency compared to the unsubstituted analogs (evident from pairs such as **2** vs. **3**, **4** vs. **5**, **10a** vs. **10c** and **11a** vs. **11c**/**11d**), although in some cases this substitution also slightly increased cytotoxicity in normal cells (e.g., **11b**, **11f**). Likewise, the presence of electron-withdrawing groups on the arylidene or heteroaryl hydrazone fragment (such as a nitro group in **10f**, **11f**, **12b**, **13b**, or halogens like Cl/Br in **10c**, **10d**, **11c**, **11d**) correlated with greater anticancer efficacy, presumably by enhancing target binding affinity or cellular uptake. The most active analogs indeed combined both structural features—a halogenated imidazole core and an electron-rich or electron-withdrawing substituent on the appended ring. For example, compound **13b**'s unique pairing of a 4′-chloro phenacyl-imidazole with a nitro-substituted heterocycle appears particularly advantageous, yielding potent tumor cell kill while sparing normal fibroblasts. By contrast, certain highly potent analogs such as **11d** and **11f** display reduced selectivity, underscoring the sensitivity of the therapeutic window to subtle structural changes. These SAR trends guided the designation of **13b** as the lead for mechanistic studies, which will proceed in U-2 OS and HeLa models to define its mode of action.

Apoptosis induction by compound 13b in U-2 OS and HeLa cells

To elucidate the mechanism underlying the cytotoxic effects of compound **13b**, we performed Annexin V-FITC/7-AAD double staining followed by flow cytometry analysis in U-2 OS and HeLa cells after 24 and 48 h of treatment (Fig. 5). Etoposide (ETP) served as a positive control for apoptosis induction.

In U-2 OS cells, compound **13b** induced a marked increase in apoptotic cell populations in a time-dependent manner (Fig. 5a). After 24 h, the proportion of early apoptotic cells increased from a baseline of 4.64–4.97% in the DMSO control to 19.1–26.5%, while late apoptotic cells increased from ~ 3% to ~ 11.7–14.7% (Fig. 5b). After 48 h, early apoptosis remained elevated (18.7–19.65%), and late apoptosis further increased to 13.0–21.05%. The total apoptotic population (early + late) reached up to ~ 40%, which was comparable to or exceeded the effect observed with ETP (early: 13.1–15.65%, late: 14.45–17.2%). Notably, a moderate increase in necrotic cells was observed at 48 h (up to 8.94%), suggesting that prolonged exposure may result in secondary necrosis following apoptosis.

In HeLa cells, compound **13b** also induced apoptosis, albeit to a lesser extent (Fig. 5c). After 24 h, early and late apoptotic populations increased modestly (early: 6.81–6.99%, late: 4.34–9.31%) compared to DMSO-treated controls (early: 2.67–3.93%, late: 1.66–2.13%) (Fig. 5d). After 48 h, early apoptosis remained elevated (6.83–

Compound	U-2 OS	HeLa	HCT-116	A-549	MRC-5
	IC$_{50}$ [μM]				
2	10.03 ± 1.58	78.16 ± 4.41	35.54 ± 1.11	39.23 ± 3.83	41.39 ± 7.39
3	6.15 ± 0.93	37.23 ± 0.93	35.15 ± 0.95	27.84 ± 2.59	31.98 ± 2.93
4	23.53 ± 2.03	95.70 ± 0.82	> 100	72.62 ± 14.28	31.22 ± 2.42
5	20.93 ± 1.65	> 100	18.70 ± 0.00	50.01 ± 29.62	40.13 ± 1.22
6	57.77 ± 7.73	> 100	81.53 ± 5.30	82.70 ± 4.81	24.25 ± 3.35
7	36.63 ± 9.58	> 100	81.51 ± 6.73	> 100	32.17 ± 4.12
8	56.50 ± 1.64	> 100	83.41 ± 1.67	85.65 ± 11.63	28.56 ± 3.16
9	39.32 ± 3.54	> 100	96.48 ± 3.08	> 100	21.33 ± 3.18
10a	11.56 ± 1.98	> 100	43.39 ± 1.30	43.02 ± 2.44	> 100
10b	11.47 ± 2.45	> 100	43.38 ± 1.34	34.63 ± 6.09	> 100
10c	7.58 ± 0.79	> 100	20.79 ± 3.81	21.21 ± 2.75	> 100
10d	9.04 ± 2.71	> 100	19.99 ± 1.45	48.46 ± 3.26	> 100
10e	12.04 ± 0.92	> 100	> 100	> 100	> 100
10f	9.42 ± 1.08	17.41 ± 2.49	11.12 ± 2.28	> 100	15.41 ± 2.19
11a	8.94 ± 2.12	18.95 ± 2.76	12.07 ± 3.24	20.90 ± 3.03	23.36 ± 4.45
11b	6.30 ± 0.14	11.58 ± 1.27	17.30 ± 2.58	12.79 ± 3.09	10.46 ± 2.84
11c	7.89 ± 0.21	10.21 ± 1.42	8.53 ± 0.73	10.77 ± 0.34	13.94 ± 1.21
11d	5.65 ± 0.50	8.31 ± 0.16	7.65 ± 1.46	5.74 ± 1.03	11.42 ± 2.14
11e	8.82 ± 1.93	24.14 ± 7.88	26.05 ± 3.58	16.94 ± 2.15	30.93 ± 5.49
11f	5.25 ± 2.00	6.53 ± 1.53	7.97 ± 1.33	9.09 ± 4.09	11.55 ± 0.53
12a	21.42 ± 6.68	> 100	41.25 ± 0.64	> 100	> 100
12b	2.71 ± 0.02	13.65 ± 0.25	16.51 ± 7.74	13.40 ± 3.23	35.45 ± 8.09
13a	12.79 ± 2.18	44.19 ± 0.91	13.12 ± 1.13	58.51 ± 4.06	31.34 ± 6.75
13b	1.57 ± 0.26	2.75 ± 0.07	10.63 ± 0.40	> 100	> 100
14	> 100	> 100	> 100	> 100	> 100
15	6.90 ± 1.87	22.65 ± 0.34	23.36 ± 5.16	45.97 ± 6.21	20.15 ± 5.52
16	> 100	> 100	> 100	> 100	> 100
17	1.51 ± 0.86	14.07 ± 2.88	12.21 ± 1.35	> 100	15.74 ± 5.86
18	8.44 ± 6.51	14.22 ± 0.49	10.16 ± 2.86	51.11 ± 13.10	> 100
19	> 100	> 100	23.59 ± 0.15	> 100	> 100
20	> 100	12.85 ± 1.00	12.57 ± 2.54	25.04 ± 3.46	89.01 ± 9.54
21	9.95 ± 2.37	8.43 ± 0.23	10.31 ± 5.60	16.39 ± 2.74	> 100
Cisplatin	8.54 ± 1.14	9.23 ± 1.23	14.15 ± 0.48	9.97 ± 0.09	> 100

Table 1. *In vitro* anticancer activity of investigated compounds (IC50 ± SD (μM)) towards non-small cell lung adenocarcinoma (A-549), cervical carcinoma (HeLa), osteosarcoma (U-2 OS), colon cancer (HCT-116), and normal lung fibroblasts (MRC-5). IC$_{50}$ value represent a concentration that inhibits 50% of cell growth.

8.98%), while late apoptosis rose to 10.47–11.5%, indicating progressive apoptotic commitment. The extent of apoptosis induction by **13b** in HeLa cells was slightly lower than that observed for ETP, which induced ~ 15–16% late apoptosis after 48 h. The proportion of necrotic cells remained low (< 4%) at all time points in both cell lines treated with **13b**, suggesting that its cytotoxic action predominantly proceeds via programmed cell death rather than primary necrosis.

To verify whether the observed apoptotic phenotype was mediated via activation of the intrinsic executioner pathway, we quantified caspase-3/7 activity following treatment with compound **13b** for 24 h and 48 h in U-2 OS and HeLa cells, using a fluorometric assay (Fig. 6). Etoposide (ETP) was employed as a positive control, and DMSO as vehicle.

In U-2 OS cells, compound **13b** significantly increased caspase-3/7 activity in a time-dependent manner (Fig. 6). After 24 h, a modest but statistically significant 1.5–1.7-fold increase was observed compared to DMSO ($p < 0.01$). At 48 h, caspase activity markedly increased to ~ 4.5–5.0-fold relative to the control ($p < 0.00001$), matching the induction observed with ETP (~ 4.2–4.6-fold). These results align with the flow cytometry data showing substantial accumulation of early and late apoptotic populations over time and strongly suggest that compound **13b** induces caspase-dependent apoptosis in osteosarcoma cells.

In HeLa cells, a similar trend was observed, though the magnitude of caspase activation was slightly lower (Fig. 6). At 24 h, treatment with **13b** led to a marginal increase (1.06–1.07-fold, not statistically significant), but at 48 h, a robust and significant ~ 2.5–2.8-fold activation was detected ($p < 0.01$). While ETP induced even stronger caspase activation (~ 4.1–6.0-fold), compound **13b** still demonstrated substantial pro-apoptotic signaling, consistent with the observed annexin V/7-AAD staining.

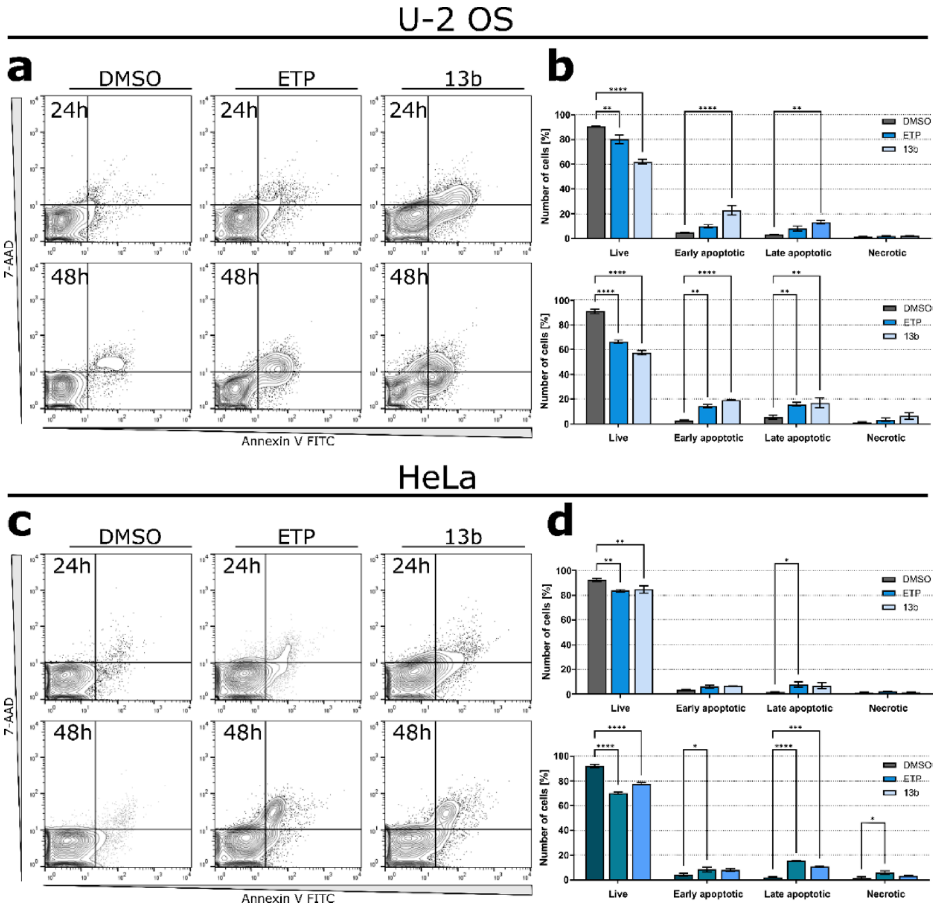

Fig. 5. Induction of apoptosis by compound **13b** in U-2 OS and HeLa cells. Representative flow cytometry dot plots illustrating Annexin V-FITC and 7-AAD staining profiles following 24- and 48-hour treatment with compound **13b**, etoposide (ETP, positive control), or vehicle (DMSO) in U- 2 OS (**a**) and HeLa (**c**) cell lines. Quantitative analysis of early and late apoptotic populations based on Annexin V/7-AAD co-staining in U-2 OS (**b**) and HeLa (**d**) cells. Bar graphs depict the percentage of cells following treatment (mean ± SEM; $n = 3$). Data represent three independent experiments. Statistical comparisons were performed using two-way ANOVA followed by Dunnett's multiple comparisons test. $^{*}p < 0.01$, $^{**}p < 0.001$, $^{***}p < 0.0001$, $^{****}p < 0.00001$ vs. vehicle control.

The caspase assay results firmly establish that the mode of cell death caused by **13b** is apoptosis involving the canonical executioner caspases. The strong fold-increase in caspase-3/7 activity, particularly in U-2 OS, suggests that **13b** likely activates the intrinsic (mitochondrial) apoptotic pathway downstream of initial damage signals. The somewhat attenuated caspase response in HeLa relative to U-2 OS is consistent with their differential sensitivity, potentially hinting at cell-specific factors such as drug uptake, metabolism, or apoptotic threshold. Notably, the concordance between Annexin V/7-AAD staining and caspase-3/7 activation provides coherent evidence that cell death elicited by **13b** proceeds predominantly through a regulated apoptotic program rather than necrosis or alternative forms of non-apoptotic cell death.

Compound 13b induces DNA damage and cytoskeletal remodeling

To further explore the cellular consequences of compound **13b**, we performed immunofluorescence staining to simultaneously assess nuclear DNA damage and cytoskeletal integrity in U-2 OS and HeLa cells. γH2AX was used as a marker of DNA double-strand breaks, while phalloidin staining enabled visualization of F-actin filament organization (Fig. 7).

In vehicle-treated controls (DMSO), U-2 OS cells exhibited a well-organized actin cytoskeleton, consisting of prominent stress fibers and cortical actin bundles, consistent with a fully spread and adherent morphology (Fig. 7). The γH2AX signal was minimal, indicating preserved genomic integrity under basal conditions. Treatment with compound **13b** for 24 h did not result in overt cytoskeletal alterations; stress fiber organization and overall cellular morphology remained comparable to controls. However, a pronounced accumulation of nuclear γH2AX foci was observed at this timepoint, indicating the onset of substantial DNA damage. After 48 h of exposure, the γH2AX signal remained elevated, suggesting sustained DNA damage. Subtle changes in actin organization were also noted, including partial disassembly and heterogeneity in stress fiber distribution.

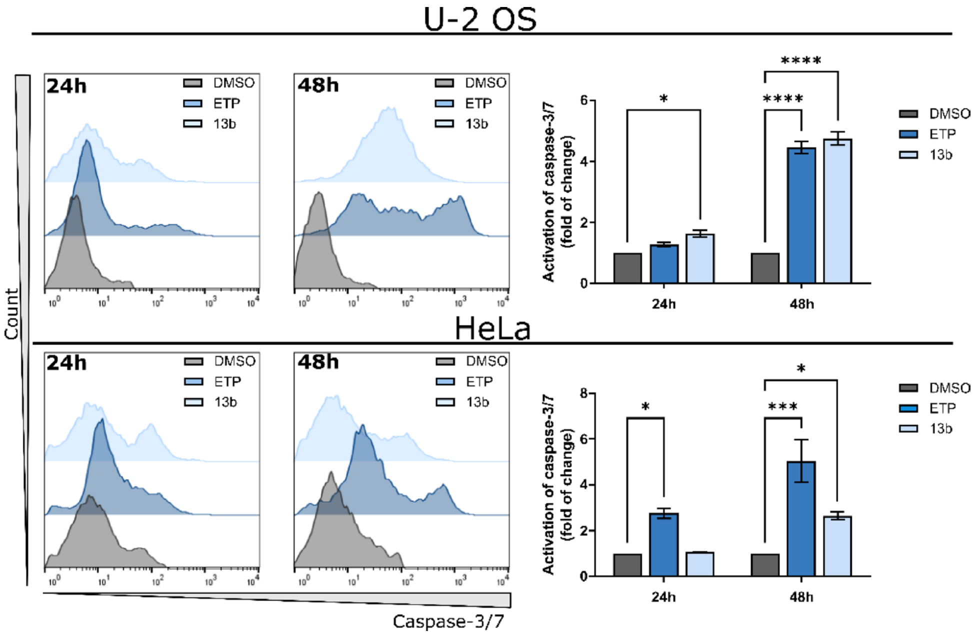

Fig. 6. Time-dependent caspase-3/7 activation in U-2 OS and HeLa cells upon treatment with compound **13b.** Representative histograms display caspase-3/7 activity measured in U-2 OS and HeLa cells following 24- and 48-hour exposure to compound **13b** or vehicle control (DMSO) (left panel). Quantitative analysis of caspase-3/7–positive cell populations is presented in the form of bar charts (right panel). Data are shown as mean values ± standard error of the mean (SEM) from three independent experiments ($n = 3$). Statistical evaluation was conducted using two-way analysis of variance (ANOVA) followed by Dunnett's multiple comparisons test. *$p < 0.01$, ***$p < 0.0001$, ****$p < 0.00001$ in comparison to the vehicle-treated group.

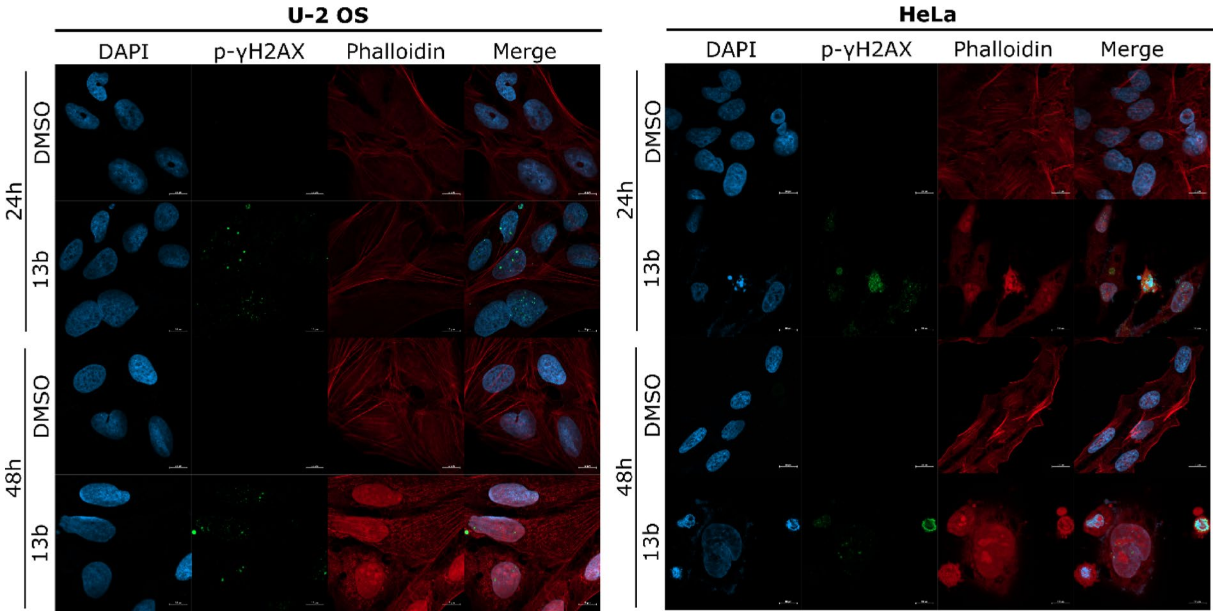

Fig. 7. Confocal imaging of γ-H2AX foci formation in U-2O S and HeLa cells following **13b** treatment. Laser scanning confocal microscopy was used to visualize DNA damage in.

Despite these alterations, most cells retained a flattened morphology, with no widespread cytoskeletal collapse or apoptotic rounding.

In contrast, HeLa cells responded to compound **13b** with more pronounced and time-dependent morphological changes (Fig. 7). Control HeLa cells displayed dense, well-aligned actin networks and negligible γH2AX staining. After 24 h of **13b** exposure, modest stress fiber fragmentation and perinuclear actin retraction were observed, although the majority of cells preserved their elongated shape. Notably, nuclear γH2AX foci were already abundant at this early stage, indicating robust activation of the DNA damage response. By 48 h, cytoskeletal integrity was severely compromised: cells exhibited a rounded morphology, disorganized F-actin staining, and partial detachment from the substratum. Nuclear γH2AX levels remained high, consistent with persistent DNA damage. Of note, one markedly enlarged cell with an abnormally large nucleus was observed, potentially reflecting mitotic slippage or nuclear dysregulation in response to unrepaired genotoxic stress[67].

These microscopy results indicate that compound **13b** induces nuclear γH2AX accumulation in cancer cells, consistent with the activation of a DNA damage response. While such signaling is not inherently synonymous with apoptosis, persistent DNA damage or failed repair may subsequently engage apoptotic pathways[68]. The early surge in γH2AX foci indicates that DNA double-strand breaks (or stalled replication forks) occur soon after treatment, which could arise either from direct DNA interaction by **13b** or indirectly from mitotic disruption and ensuing genomic instability[69–71]. The observed cellular morphologies further support an apoptotic mechanism: the progressive loss of actin stress fibers, cell body contraction, and membrane blebbing (especially in HeLa) are classic features of cells undergoing apoptosis[72,73]. The fact that U-2 OS cells retained their cytoskeleton longer than HeLa may reflect differences in how quickly each cell type commits to apoptosis or how **13b**'s mechanism impacts their cytoskeletal regulators. Importantly, the presence of a giant polyploid-like cell in treated HeLa suggests that **13b** might interfere with normal mitotic progression—hinting that its cytotoxic action could involve mitotic arrest or spindle damage (consistent with the known antimitotic effects of TMP-bearing compounds)[42]. Such a cell could result from mitotic slippage, where a cell escapes a failed division attempt, further implicating a mechanism of action tied to disruption of the cell cycle[74,75].

U-2 OS and HeLa cells after 24- and 48-hour incubation with compound **13b**. Representative high-resolution images show γ-H2AX phosphorylation sites (green), cytoskeletal F-actin structures (red), and nuclei stained with DAPI (blue). Etoposide (ETP) and DMSO were used as positive and negative controls, respectively. Scale bars represent 10 µm.

Compound 13b impairs 3D spheroid growth in HeLa and U-2 OS cells in a dose-dependent manner

To further investigate the sustained antiproliferative activity of compound **13b** under physiologically relevant conditions, we employed 3D spheroid models derived from HeLa and U-2 OS cells. Spheroids were generated using ultra-low-attachment conditions and exposed to increasing concentrations of compound **13b** (5–50 µM). Bright-field microscopy was used to monitor spheroid growth over a five-day period, and morphometric parameters—including spheroid area and diameter—were quantitatively assessed at the experimental endpoint (Fig. 8).

In HeLa spheroids, compound **13b** elicited a progressive, concentration-dependent reduction in both area and diameter (Fig. 8a–b). At 10 µM, a modest decrease in mean spheroid area was observed (140,235 µm^2 vs. >160,000 µm^2 in controls), with only a slight change in average diameter. At higher concentrations (25 µM and 50 µM), the reduction became more pronounced, with spheroid areas falling below 110,000 µm^2. Morphologically, bright-field images revealed a visible loss of compactness, suggesting impaired cell proliferation, disruption of intercellular adhesion, and potential activation of cell-death pathways.

The effects of compound **13b** were even more pronounced in U-2 OS spheroids (Fig. 8c,d). Already at 10 µM, a marked decline in spheroid size was detected (mean area ~ 75,000–85,000 µm^2), corresponding to > 60% reduction relative to vehicle. At 50 µM, most spheroids failed to maintain structural integrity, appearing flattened or fragmented in morphology. Quantitative analysis confirmed that spheroid diameter decreased from ~ 470 µm in controls to ~ 250–300 µm following treatment. The loss of spheroid cohesion and compactness points to disrupted proliferation and cell–cell interactions, in line with observations from 2D cytoskeletal staining (Fig. 7). Importantly, the ability of **13b** to penetrate and suppress multicellular spheroids suggests it can overcome some diffusion and microenvironment barriers that often render tumors less responsive to therapy[73]. The near-complete collapse of U-2 OS spheroids at higher concentrations of **13b** highlights the compound's potential efficacy against osteosarcoma in a 3D tumor context. HeLa spheroids, while more resilient than U-2 OS, were still significantly stunted by **13b** in a concentration-dependent manner, indicating that even for less sensitive cell types, sufficiently high concentrations of **13b** can achieve strong antiproliferative effects in 3D.

Given the pronounced growth inhibition in U-2 OS spheroids, we next investigated whether the observed effects were attributable to apoptotic cell death. Fluorescence-based assays were performed to detect phosphatidylserine externalization and membrane permeabilization—hallmarks of early and late apoptosis, respectively—using Annexin V-FITC (green) and propidium iodide (PI, red), with nuclear staining by DAPI (blue) (Fig. 9a). In untreated spheroids, Annexin V and PI signals were negligible, consistent with high cell viability and preserved architecture. In contrast, compound **13b** treatment resulted in a concentration-dependent increase in both apoptotic markers. At 10 µM, Annexin V fluorescence became pronounced, particularly at the spheroid periphery, indicating early apoptotic onset. At 25 µM and 50 µM, co-localized Annexin V and PI signals were detected throughout the spheroid structure, indicative of advanced apoptotic progression and possible secondary necrosis. Quantitative fluorescence analysis across multiple spheroids confirmed these observations (Fig. 9b). Annexin V signal increased significantly at 10 µM and above, while PI signal rose sharply at 25 µM and 50 µM ($p < 0.01$ vs. control), supporting a dose-dependent activation of apoptosis by compound **13b**. These results corroborate that **13b** induces apoptosis in 3D cultures similarly as in 2D, and they highlight a diffusion-related gradient in spheroid penetration. The finding that higher concentrations of **13b** achieve uniform induction of apoptosis throughout the spheroid mass underscores the importance of adequate drug delivery in solid tumor contexts. Overall, the spheroid experiments strengthen the translational relevance of **13b**'s anticancer activity by showing that its effects are not limited to monolayer cultures but extend to more realistic tumor models.

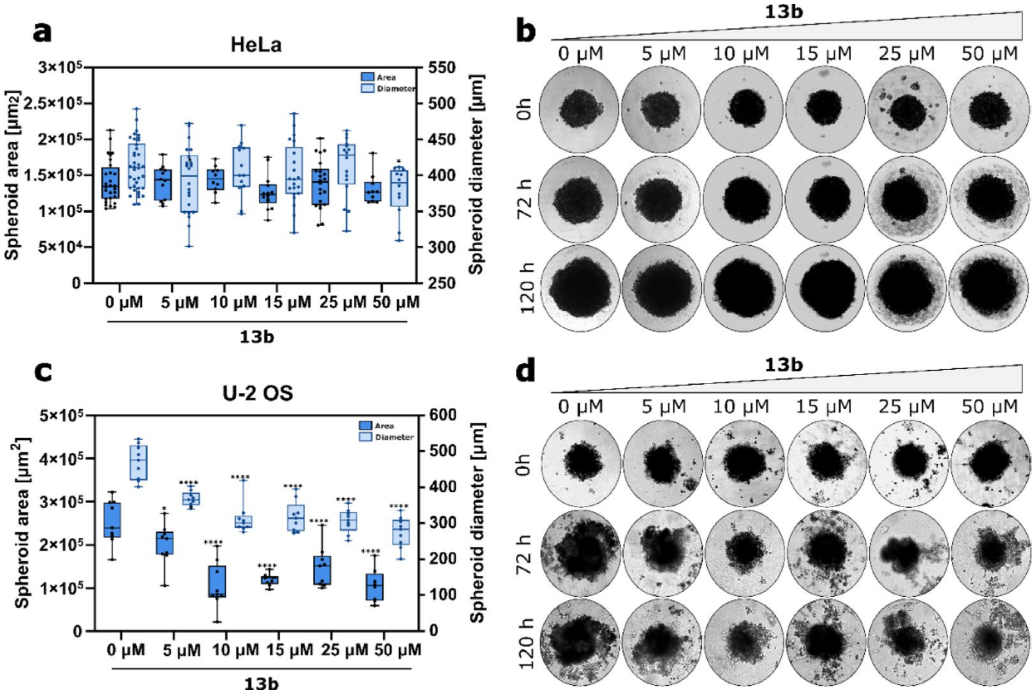

Fig. 8. Impact of compound **13b** on 3D spheroid development in HeLa and U-2 OS cells over a 5-days period. Quantitative data illustrate changes in spheroid size, expressed as area and diameter (mean ± SEM), for HeLa (**a**) and U-2 OS (**c**) cell-derived spheroids following treatment. Measurements were performed after 5 days of incubation with compound **13b**. Bright-field microscopy images of spheroids generated from HeLa (**b**) and U-2 OS (**d**) cells were captured at selected time points during 72-hour incubation with compound **13b** at concentrations of 0, 5, 10, 15, 25, and 50 µM. Statistical significance was evaluated using two-way ANOVA followed by Dunnett's post hoc test. *$p < 0.01$, **$p < 0.001$, ***$p < 0.0001$, ****$p < 0.00001$ compared to vehicle-treated controls.

Physicochemical properties and drug-likeness analysis

To better characterize the drug-like properties of the synthesized thioimidazole–TMP conjugates, we performed an *in silico* analysis of key physicochemical descriptors using the SwissADME platform (Table 2)[76]. The analysis included molecular weight (MW), hydrogen bond donors (HBD), hydrogen bond acceptors (HBA), lipophilicity (consensus logP), topological polar surface area (TPSA), number of rotatable bonds (NRB), solubility class, and bioavailability score—parameters commonly used at the early stages of small-molecule drug discovery[76,77].

All compounds in the series comply with Lipinski's Rule of Five and display a consistent physicochemical profile characterized by limited hydrogen-bonding capacity and moderate lipophilicity[78]. Consensus logP values fall within a narrow range (approximately 2.3–4.7), indicating a balanced polarity–lipophilicity relationship compatible with cellular uptake. Importantly, none of the compounds showed Lipinski rule violations, supporting the overall drug-like nature of the hybrid scaffold.

Assessment based on Veber's criteria showed that some derivatives exceed the recommended thresholds for TPSA and/or the number of rotatable bonds[79]. Such deviations are frequently observed for cytotoxic anticancer agents and do not necessarily exclude biological activity, particularly when non-oral routes of administration or facilitated cellular uptake mechanisms are considered[80]. Notably, several of the most active compounds retained strong antiproliferative effects despite these deviations.

According to SwissADME predictions, most compounds are classified as moderately to poorly soluble, a feature commonly reported for lipophilic heterocyclic anticancer molecules[81]. Nevertheless, all analyzed derivatives share a bioavailability score of 0.55, suggesting that their physicochemical profiles remain suitable for further optimization[76]. Taken together, these data indicate that the thioimidazole–TMP conjugates occupy a recognized drug-like chemical space and represent viable lead structures for continued anticancer drug development.

Conclusion

In the present work, we successfully synthesized a panel of novel thioimidazole derivatives incorporating the TMP pharmacophore and demonstrated their potential anticancer properties through comprehensive *in vitro* evaluations. The convergence of these two privileged motifs (a sulfur-containing imidazole core and a TMP-substituted aromatic group) was designed to maximize anticancer efficacy, and our results indeed showcase strong cytotoxic activity for several hybrid compounds, with compound **13b** emerging as a standout lead. Compound **13b**, in particular, exhibited sub-micromolar potency against multiple cancer cell lines while sparing normal fibroblasts, and it induced robust apoptosis, DNA damage, and growth suppression even in 3D tumor

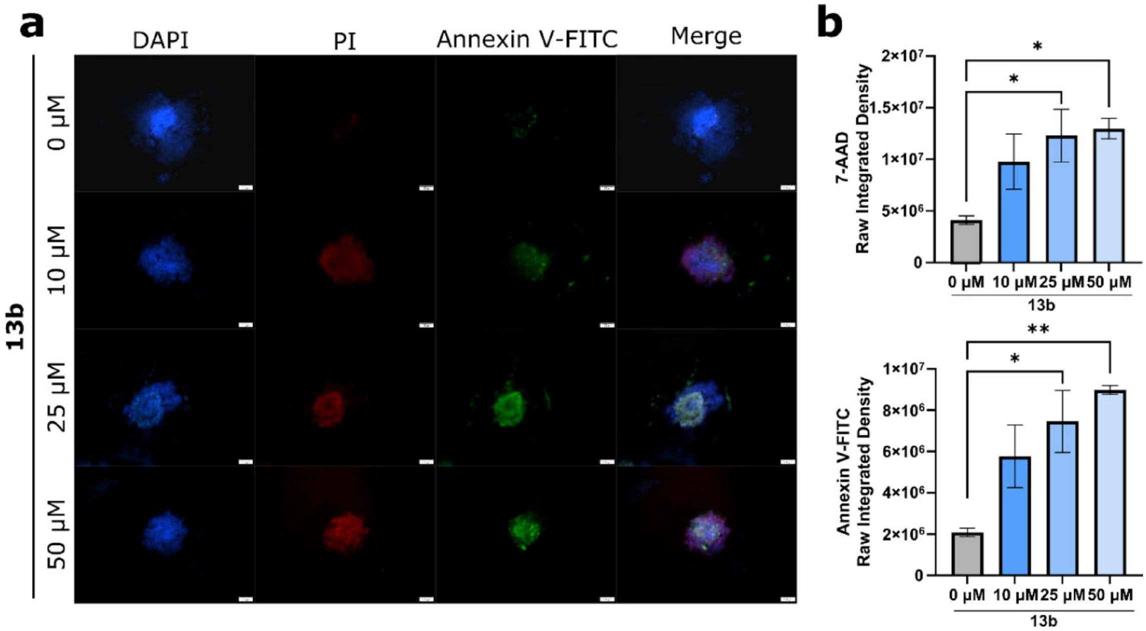

Fig. 9. Fluorescence-based analysis of apoptosis in U-2 OS spheroids after 72-hour treatment with compound **13b.** (**a**) Representative fluorescence microscopy images of U-2 OS spheroids incubated for 72 h with increasing concentrations of compound **13b**. Staining includes DAPI (nuclei, blue), propidium iodide (PI; late apoptosis/necrosis, red), and Annexin V-FITC (early apoptosis, green). Scale bars: 100 µm. (**b**) Quantification of total fluorescence intensity corresponding to Annexin V-FITC and PI signals across 10 individual spheroids per condition. Results are expressed as mean ± SEM. Statistical analysis was performed using one-way ANOVA followed by Dunnett's post hoc test. $^{*}p < 0.01$, $^{**}p < 0.001$ vs. untreated control.

spheroid models. These findings underscore the success of our hybrid scaffold strategy in achieving potent and selective antitumor activity.

Although the precise molecular targets of our thioimidazole–TMP hybrids remain to be elucidated, the observed induction of DNA damage and apoptosis aligns well with the known mechanisms of TMP-based antimitotic agents (such as combretastatins that disrupt microtubules and trigger DNA damage response[49]. By analogy, it is plausible that compound **13b** and its analogues interfere with critical cellular targets or pathways (for example, tubulin dynamics, topoisomerases, or other enzymes identified for TMP compound[42], leading to mitotic arrest and consequent DNA breakage. However, it must be emphasized that these mechanistic considerations are preliminary; dedicated studies are required to identify the exact protein targets and pathways affected by **13b.**

Importantly, the biological activity of the thioimidazole–TMP hybrids was complemented by an *in silico* physicochemical and drug-likeness assessment, demonstrating that the compounds occupy a recognized drug-like chemical space compatible with small-molecule lead development. This analysis supports the notion that incorporation of the thioimidazole fragment does not compromise fundamental drug-like characteristics of the TMP-based scaffold, thereby strengthening the translational relevance of the observed anticancer effects.

Furthermore, our data confirm that hybridization of the thioimidazole core with a TMP substituent yields compounds capable of penetrating multicellular tumor spheroids and triggering cytotoxic responses under physiologically relevant 3D conditions. As spheroid models more closely recapitulate the architecture, cell–cell interactions, and microenvironmental gradients of solid tumors than conventional 2D monolayers, the observed activity further supports the robustness of this scaffold for anticancer research[73].

Taken together, this study provides a compelling rationale for the continued exploration of TMP–imidazole, and particularly thioimidazole, hybrids as anticancer agents. By combining two privileged structural motifs—imidazole, which offers versatile binding interactions and favorable physicochemical properties, and TMP, which confers multi-target cytotoxic activity—we establish a rational framework for the design of multifunctional anticancer leads. Future work will focus on further optimization of compound **13b** and related analogues with respect to drug-like properties and in vivo performance, as well as detailed mechanistic studies aimed at identifying their direct molecular targets. The results presented herein lay a solid foundation for advancing this new class of thioimidazole–TMP conjugates toward preclinical evaluation in oncology.

Methods

Cell culture

In this study, a panel of five human cell lines was employed, including four cancer-derived lines—A-549 lung adenocarcinoma (CCL-185), HCT-116 colorectal carcinoma (CCL-247), HeLa cervical carcinoma (CCL-2), and U-2 OS osteosarcoma (HTB-96)—as well as one non-cancerous control, MRC-5 normal human lung fibroblasts

Molecule	HBD	HBA	logP	TPSA (Å^2)	NRB	Lipinski violations	Veber compliant*	Bioavailability score
2	1	4	2.74	56.79	7	0	Yes	0.55
3	1	4	3.22	56.79	7	0	Yes	0.55
4	0	4	3.25	84.31	5	0	Yes	0.55
5	0	4	3.82	84.31	5	0	Yes	0.55
6	0	6	3.46	97.11	9	0	Yes	0.55
7	0	6	3.98	97.11	9	0	Yes	0.55
8	2	6	2.30	125.93	7	0	Yes	0.55
9	2	6	2.83	125.93	7	0	Yes	0.55
10a	1	6	4.18	112.27	7	0	Yes	0.55
10b	1	7	4.43	112.27	7	0	Yes	0.55
10c	1	6	4.67	112.27	7	0	Yes	0.55
10d	1	6	4.74	112.27	7	0	Yes	0.55
10e	1	6	4.11	115.51	9	0	Yes	0.55
10f	1	8	3.43	158.09	9	0	No	0.55
11a	1	6	4.69	112.27	7	0	Yes	0.55
11b	1	8	3.69	154.85	9	0	No	0.55
11c	2	6	3.86	132.99	11	0	No	0.55
11d	2	8	3.18	175.57	11	0	No	0.55
11e	2	6	4.16	140.38	12	0	No	0.55
11f	2	6	4.18	132.99	12	0	No	0.55
12a	2	6	3.65	140.38	11	0	No	0.55
12b	2	8	2.98	182.96	12	0	No	0.55
13a	2	6	3.67	147.77	11	0	No	0.55
13b	2	8	3.28	190.35	12	0	No	0.55
14	2	6	4.47	147.77	11	0	No	0.55
15	2	6	4.49	147.77	11	0	No	0.55
16	2	6	4.47	147.77	11	0	No	0.55
17	2	6	4.49	147.77	11	0	No	0.55
18	1	6	3.40	123.79	9	0	Yes	0.55
19	1	6	3.94	123.79	9	0	Yes	0.55
20	1	6	3.92	131.18	10	0	Yes	0.55
21	1	6	4.46	131.18	10	0	Yes	0.55

Table 2. *In Silico* physicochemical and drug-likeness profiling of the synthesized thioimidazole–TMP conjugates. * Veber compliant: TPSA ≤ 140 Å^2 and NRB ≤ 10.

(CCL-171), to evaluate both cytotoxicity and selectivity of the tested compounds. All cell lines were obtained from the American Type Culture Collection (ATCC, Manassas, VA, USA). A-549 cells were cultured in RPMI-1640 medium, while HCT-116 and U-2 OS cells were maintained in McCoy's 5 A medium. HeLa cells were grown in Dulbecco's Modified Eagle Medium (DMEM), and MRC-5 fibroblasts were cultured in Minimum Essential Medium (MEM). All culture media were supplemented with 10% fetal bovine serum (FBS), 2 mM L-glutamine, and antibiotics (100 U/mL penicillin and 100 µg/mL streptomycin). Cell cultures were maintained at 37 °C in a humidified atmosphere containing 5% CO_2. Subculturing was performed at 70–80% confluency using standard trypsin-EDTA treatment, and routine testing for mycoplasma contamination was conducted.

Cell viability assay

Cellular metabolic activity was quantified using the MTT colorimetric assay (Sigma-Aldrich), which indirectly reflects cell viability. Cells were seeded into 96-well flat-bottom plates and incubated overnight to allow for proper attachment. The following day, cells were exposed to a range of compound concentrations (1-100 µM) for 72 h. DMSO-treated wells served as vehicle controls. Upon completion of the treatment period, MTT reagent was added at a final concentration of 0.4 mg/mL, and plates were incubated for 2–3 h at 37 °C to allow for formazan crystal formation. The supernatant was then aspirated, and 100 µL of DMSO was added to each well to solubilize the crystals. Absorbance was measured at 450 nm using an ASYS UVM340 microplate reader. The half-maximal inhibitory concentration (IC_{50}) values were calculated by nonlinear regression of dose-response curves using GraphPad Prism 9 software. All treatments were conducted in triplicate, and data represent the mean ± SEM of three independent biological replicates to ensure analytical robustness.

Apoptosis detection and caspase-3/7 activation assay

To investigate apoptosis induction by the tested compounds, HeLa and U-2 OS cells were seeded onto standard tissue culture plates and incubated overnight to allow cell adherence. On the following day, cells were treated with the compound at its IC_{50} concentration for 24–48 h. Etoposide (ETP) was used as a positive control to validate assay performance. Following treatment, cells were detached using trypsin-EDTA, washed twice with phosphate-buffered saline (PBS), and stained according to the manufacturers' protocols. Early apoptotic cells were labeled using Annexin V-FITC (Thermo Fisher Scientific; #A13199), which binds to externalized phosphatidylserine residues. Dead and late apoptotic cells were identified by staining with 7-aminoactinomycin D (7-AAD), allowing discrimination between viable, early apoptotic, late apoptotic, and necrotic cell populations. In parallel, caspase-3/7 enzymatic activity was detected using the CellEvent™ Caspase-3/7 Green Flow Cytometry Assay Kit (Thermo Fisher Scientific; #C10427), which selectively fluoresces in cells with activated executioner caspases. Flow cytometric analysis was conducted immediately after staining using a Guava easyCyte 8 flow cytometer (Merck Millipore). Data were analyzed with FlowJo v10 software (BD Life Sciences). All experiments were performed in triplicate, and representative results from at least three independent experiments are reported.

Immunofluorescence analysis

To assess DNA damage and cytoskeletal alterations induced by the tested compounds, U-2 OS and HeLa cells were seeded onto sterile glass coverslips and allowed to adhere for 24 h under standard culture conditions. Cells were subsequently treated with compound **13b** at concentrations corresponding to their respective IC_{50} values for 24 and 48 h. Following treatment, cells were gently washed twice with phosphate-buffered saline (PBS) and fixed in 4% paraformaldehyde (Sigma-Aldrich) for 10 min at room temperature. Permeabilization was performed using 0.25% Triton X-100 (Sigma-Aldrich) in PBS for 15 min. After permeabilization, cells were rinsed twice in PBS (5 min each) and incubated with 3% bovine serum albumin (BSA; Sigma-Aldrich) in PBS for 1 h to block nonspecific binding sites. Cells were then incubated for 1 h at 37 °C with an Alexa Fluor 488-conjugated anti-γH2AX (Ser139) monoclonal antibody (1:250; BioLegend, #613406) diluted in 3% BSA in PBS-T (PBS containing 0.1% Tween-20). To visualize the actin cytoskeleton, cells were co-stained with phalloidin conjugated to a fluorophore (A22287; Thermo Fisher Scientific) under the same conditions. After antibody incubation, coverslips were washed twice with PBS-T, counterstained with DAPI (0.25 µg/ml; Sigma-Aldrich) to label nuclear DNA, and mounted onto glass slides using an antifade medium. Imaging was performed on a Zeiss LSM 800 inverted confocal laser scanning microscope equipped with an Airyscan detector and a 63×/1.4 NA Plan-Apochromat oil immersion objective (Carl Zeiss). All imaging settings were maintained consistently across experimental conditions to ensure valid comparisons.

3D spheroid formation assay.

Three-dimensional (3D) multicellular tumor spheroids were generated using the 3D Petri Dish® platform (MicroTissues®, #12–256), following the manufacturer's guidelines. A sterile 2% agarose solution prepared in physiological saline was liquefied by heat and poured into micromolds under aseptic conditions. After polymerization at room temperature, agarose constructs were transferred to 12-well culture plates and equilibrated with complete growth medium. U-2 OS cells were seeded into the molds using serum-free medium and allowed to sediment into the microwells for 1–2 h at 37 °C to promote uniform spheroid formation. Once aggregates had formed, an appropriate volume of complete medium was added to ensure full immersion of the gel matrices. After 72 h, spheroids were treated with compound **13b** at concentrations of 5, 10, 15, 25, or 50 µM. Vehicle-treated controls (0.5% v/v DMSO in PBS) were included for comparison. Cultures were maintained under standard incubator conditions (37 °C, 5% CO_2, humidified atmosphere) and monitored over a period of 120 h. Bright-field images were acquired at three key time points (0 h, 72 h, and 120 h) using an Olympus CellVivo inverted microscope system optimized for long-term live-cell imaging. Morphometric parameters, including spheroid area and diameter, were measured using Olympus CellSens imaging software. Data were derived from multiple independent spheroids per condition to ensure reproducibility and statistical robustness.

Apoptosis detection by fluorescence imaging in 3D spheroids

To evaluate the pro-apoptotic activity of compound **13b** in a structurally relevant 3D tumor model, multicellular spheroids of U-2 OS cells were formed using ultra-low attachment (ULA) 96-well plates (Corning® Costar®, #7007). Cells were seeded in serum-free conditions and allowed to spontaneously aggregate over a 72-hour period in a humidified incubator at 37 °C and 5% CO_2. After this pre-incubation step, the medium was carefully exchanged for complete growth medium supplemented with compound **13b** at final concentrations of 10, 25, or 50 µM, or with vehicle control (0.5% DMSO in PBS). The treatment phase lasted an additional 72 h under identical environmental conditions. Following compound exposure, spheroids were stained to visualize apoptotic and necrotic processes. The staining protocol employed a mixture of 4′,6-diamidino-2-phenylindole (DAPI, 1 µg/mL; Sigma-Aldrich) to identify cell nuclei, propidium iodide (PI, 10 µg/mL; Sigma-Aldrich) to detect loss of membrane integrity characteristic of late apoptosis and necrosis, and Annexin V conjugated to fluorescein isothiocyanate (FITC; 5 µL per 100 µL; Thermo Fisher Scientific, #A13199) to label externalized phosphatidylserine, a hallmark of early apoptotic events. Spheroids were incubated with the staining solution for 1 h at 37 °C without agitation to preserve their architecture. After staining, spheroids were washed gently with phosphate-buffered saline (PBS) to remove excess reagents and immediately subjected to fluorescence imaging. Microscopy was performed using an Olympus CellVivo inverted system equipped for live-cell imaging. Identical acquisition settings were used across all samples to ensure reliable comparative analysis. Fluorescence quantification was carried out using ImageJ software by measuring the integrated intensity of Annexin V-FITC and PI signals across 10 individual spheroids per condition. Data are presented as mean values with associated standard errors (mean ± SEM).

General procedures

Reagents and solvents were purchased from Sigma-Aldrich (St. Louis, MO, USA) and used without further purification. The reaction course and purity of the synthesized compounds were monitored by TLC using aluminium plates pre-coated with Silica gel with F254 nm (Merck KGaA, Darmstadt, Germany). Melting points were determined with a B-540 melting point analyser (Büchi Corporation, New Castle, DE, USA) and are uncorrected. IR spectra (ν, cm^{-1}) were recorded on a Perkin–Elmer Spectrum BX FT–IR spectrometer (Perkin–Elmer Inc., Waltham, MA, USA) using KBr pellets. NMR spectra were recorded on a Brucker Avance III (400, 101 MHz) spectrometer (Bruker BioSpin AG, Fällanden, Switzerland). Chemical shifts were reported in (*δ*) ppm relative to tetramethylsilane (TMS) with the residual solvent as internal reference ([D_6]DMSO, *δ* = 2.50 ppm for^{1}H and δ = 39.5 ppm for^{13}C). Data are reported as follows: chemical shift, multiplicity, coupling constant [Hz], integration and assignment. Elemental analyses (C, H, N) were conducted using the Elemental Analyzer CE-440 (Exeter Analytical, Inc., North Chelmsford, MA, USA), their results were found to be in good agreement (± 0.3%) with the calculated values.

Synthesis

General procedure for Preparation of aminoketones 2,3

Starting amine **1** (3.02 g, 16.5 mmol) was dissolved in methanol (20 mL) by heating. The solution was cooled to room temperature, and sodium bicarbonate (2.49 g, 29.7 mmol) was added. The resulting mixture was stirred for 10 min. Phenacyl bromide or 4-chlorophenacyl bromide (19.8 mmol), previously dissolved in methanol (40 mL), was added dropwise to the reaction mixture. The reaction was stirred for 5 h at room temperature. The resulting precipitate was filtered off, washed with methanol and diethyl ether, and dried. Compounds **2**, **3** was purified via recrystallization from propan-2-ol.

1-Phenyl-2-((3,4,5-trimethoxyphenyl)amino)ethan-1-one (**2**) Yellow solid, yield: 3.62 g (73%) mp 138–140 °C. ^{1}H NMR (400 MHz, DMSO-d_6): δ 3.53 (s, 3 H, OCH_3) and 3.71 (s, 6 H, 2x OCH_3), 4.67 (d, *J* = 5.3 Hz, 2 H, CH_2), 5.62 (t, *J* = 5.4 Hz, 1H, NH), 7.57 (t, *J* = 7.5 Hz, 2 H, H_{Ar}), 7.64 − 7.71 (m, 1H, H_{Ar}), 8.09 (d, *J* = 7.7 Hz, 2 H, H_{Ar}). ^{13}C NMR (101 MHz, DMSO-d_6): δ 50.4 (CH_2), 55.6, 60.2 (3x OCH_3), 90.5, 127.9, 128.8, 128.9, 133.6, 144.8, 153.4 (C_{Ar}), 196.8 (C = O). IR (KBr): ν_{max} = 3420 (NH), 1683 (C = O) cm^{-1}. Anal. Calcd. for $C_{17}H_{19}NO_4$, %: C 67.76; H 6.36; N 4.65. Found: C 67.56; H 6.18; N 4.47.

1-(4-Chlorophenyl)-2-((3,4,5-trimethoxyphenyl)amino)ethan-1-one (**3**) Sandy solid, yield: 3.69 g (100%) mp 158–160 °C. ^{1}H NMR (400 MHz, DMSO-d_6): δ 3.53 (s, 3 H, OCH_3) and 3.70 (s, 6 H, 2x OCH_3), 4.65 (d, *J* = 5.3 Hz, 2 H, CH_2), 5.63 (t, *J* = 5.4 Hz, 1H, NH), 6.04 (s, 2 H, H_{Ar}), 7.64 (d, *J* = 8.2 Hz, 2 H, H_{Ar}), 8.09 (d, *J* = 8.2 Hz, 2 H, H_{Ar}). ^{13}C NMR (101 MHz, DMSO-d_6): δ 49.4 (CH_2), 55.6, 59.9 (3x OCH_3), 111.2, 114.9, 116.9, 118.0, 122.8, 129.5, 141.1, 141.7, 151.8, 162.6, 164.4 (C_{Ar}), 195.8 (C = O). IR (KBr): ν_{max} = 3371 (NH), 1691 (C = O) cm^{-1}. Anal. Calcd. for $C_{17}H_{18}ClNO_4$, %: C 60.81; H 5.40; N 4.17. Found: C 59.84; H 5.23; N 3.95.

General procedure for Preparation of compounds 4, 5

Compounds **2** or **3** (4.5 mmol) and potassium thiocyanate (6.7 mmol,) were added to 10% HCl (45 ml) and heated under reflux for 1 hours[31]. The mixture was cooled to room temperature and resulting precipitate filtered off and thoroughly washed with water, propan-2-ol and diethyl ether. Final compounds **4** and **5** was purified via recrystallization from a mixture of propan-2-ol and water.

4-Phenyl-1-(3,4,5-trimethoxyphenyl)-1 H-imidazole-2-thiol (**4**) White solid, yield: 1.03 g (67%) mp 224–226 °C. ^{1}H NMR (400 MHz, DMSO-d_6): δ 3.71 (s, 3 H, OCH_3), and 3.82 (s, 6 H, 2x OCH_3), 7.08 (s, 2 H, H_{Ar}), 7.27 − 7.34 (m, 1H, H_{Ar}), 7.43 (t, *J* = 7.6 Hz, 2 H, H_{Ar}), 7.76 (d, *J* = 7.7 Hz, 2 H, H_{Ar}), 7.86 (s, 1H, NCH), 12.96 (s, 1H, SH). ^{13}C NMR (101 MHz, DMSO-d_6): δ 56.2, 60.1 (3x OCH_3), 103.7, 116.3, 124.2, 127.8, 127.9, 128.1, 128.9, 133.4, 136.7, 152.6, 162.5 (C_{Ar}). IR (KBr): ν_{max} = 2726 (SH), 1599 (C = N) cm^{-1}. Anal. Calcd. for $C_{18}H_{18}N_2O_3S$, %: C 63.14; H 5.30; N 8.18. Found: C 62.95; H 5.17; N 7.96.

4-(4-Chlorophenyl)-1-(3,4,5-trimethoxyphenyl)-1 H-imidazole-2-thiol (**5**) White solid, yield: 1.19 g (70%) mp 246–248 °C. ^{1}H NMR (400 MHz, DMSO-d_6): δ 3.71 (s, 3 H, OCH_3), and 3.82 (s, 6 H, 2x OCH_3), 7.07 (s, 2 H, H_{Ar}), 7.50 and 7.78 (2t, *J* = 8.3 Hz, 2 H, H_{Ar}), 7.91 (s, 1H, NCH), 13.00 (s, 1H, SH). ^{13}C NMR (101 MHz, DMSO-d_6): δ 56.2, 60.1 (3x OCH_3), 103.7, 116.9, 125.9, 126.7, 127.0, 128.9, 132.2, 133.3, 136.8, 152.6, 162.7 (C_{Ar}). IR (KBr): ν_{max} = 2724 (SH), 1597 (C = N) cm^{-1}. Anal. Calcd. for $C_{18}H_{17}ClN_2O_3S$, %: C 57.37; H 4.55; N 7.43. Found: C 57.18; H 4.21; N 7.19.

General procedure for Preparation of esters 6, 7

Compounds **4** or **5** (0.5 g, 1.5 mmol) was dissolved in ethanol (30 ml) after which potassium carbonate (0.16 g, 1.2 mmol) and methyl bromoacetate (0.46 g, 3 mmol) was added in a dropwise manner[31]. Mixture was heated under reflux for 1 h and quickly filtered. Half of the filtrate was evaporated off and left-over mixture was cooled down and left-over night for precipitation to occur. Precipitate was filtered off and washed with cold propan-2-ol. Products **6** and **7** was purified via recrystallization from propan-2-ol.

Methyl 2-((4-phenyl-1-(3,4,5-trimethoxyphenyl)-1 H-imidazol-2-yl)thio)acetate (**6**) White solid, yield: 0.62 g (100%) mp 120–122 °C. ^{1}H NMR (400 MHz, DMSO-d_6): δ 3.66, 3.72 and 3.84 (3s, 12 H, 4x OCH_3), 4.08 (s, 2 H, CH_2), 6.85 (s, 2 H, H_{Ar}), 7.23 and 7.38 (2t, *J* = 7.6 Hz, 3 H, H_{Ar}), 7.78 (d, *J* = 7.6 Hz, 2 H, H_{Ar}), 8.02 (s, 1H, NCH). ^{13}C NMR (101 MHz, DMSO-d_6): δ 34.7 (CH_2), 52.3, 56.3, 60.2 (4x OCH_3), 102.8, 119.3, 124.2, 126.7, 128.5, 128.6, 132.2, 133.5, 137.2, 140.9, 153.2 (C_{Ar}) 169.4 (C = O). IR (KBr): ν_{max} = 1719 (C = O), 1596 (C = N) cm^{-1}. Anal. Calcd. for $C_{21}H_{22}N_2O_5S$, %: C 60.86; H 5.35; N 6.76. Found C 60.65; H 5.17; N 6.56.

Methyl 2-((4-(4-chlorophenyl)-1-(3,4,5-trimethoxyphenyl)-1 H-imidazol-2-yl)thio)acetate (**7**) White solid, yield: 0.52 g (78%) mp 128–130 °C. ^{1}H NMR (400 MHz, DMSO-d$_6$): δ 3.65, 3.72 and 3.84 (3s, 12 H, 4x OCH$_3$), 4.07 (s, 2 H, CH$_2$),6.85 (s, 2 H, H$_{Ar}$), 7.44 and 7.79 (2t, J = 8.2 Hz, 2 H, H$_{Ar}$), 8.09 (s, 1H, NCH). ^{13}C NMR (101 MHz, DMSO-d$_6$): δ 34.6 (CH$_2$), 52.3, 56.3, 60.2 (4x OCH$_3$), 102.8, 119.8, 125.8, 128.5, 128.6, 130.9, 132.0, 132.5, 137.3, 139.7, 141.3, 153.2 (C$_{Ar}$) 169.3 (C = O). IR (KBr): ν_{max} = 1744 (C = O), 1594 (C = N) cm^{-1}. Anal. Calcd. for $C_{21}H_{21}ClN_2O_5S$, %: C 56.19; H 4.72; N 6.24. Found: C 55.92; H 4.53; N 6.03.

General procedure for Preparation of Hydrazides 8, 9

To a cooled solution of methyl ester **6** or **7** (2.98 g, 7.2 mmol) in 2-propanol (56 mL), hydrazine monohydrate (2.10 g, 42 mmol) was added, and the mixture was heated at reflux for 5 h[82]. After completion of the reaction (TLC), the mixture was cooled to room temperature, and the obtained precipitate was filtered off, washed with propan-2-ol, and recrystallized from 2-propanol to give the titles compounds **8** and **9**.

2-((4-Phenyl-1-(3,4,5-trimethoxyphenyl)-1 H-imidazol-2-yl)thio)acetohydrazide (**8**) White solid, yield: 2.93 g (98%) mp 160–162 °C. ^{1}H NMR (400 MHz, DMSO-d$_6$): δ 3.72 (s, 3 H, OCH$_3$), and 3.84 (s, 6 H, 2x OCH$_3$), 3.88 (s, 2 H, CH$_2$), 4.33 (br. s., 2 H, NH$_2$), 6.87 (s, 2 H, H$_{Ar}$), 7.24 and 7.39 (2t, J = 7.6 Hz, 3 H, H$_{Ar}$), 7.82 (d, J = 7.6 Hz, 2 H, H$_{Ar}$), 8.02 (s, 1H, NCH), 9.41 (s, 1H, NH). ^{13}C NMR (101 MHz, DMSO-d$_6$): δ 35.1 (CH$_2$), 56.3, 60.2 (3x OCH$_3$), 103.1, 119.4, 124.4, 126.8, 128.6, 132.3, 133.6, 137.2, 140.8, 141.4, 153.1 (C$_{Ar}$) 166.8 (C = O). IR (KBr): ν_{max} = 3230, 3125 (NH2, NH), 1673 (C = O), 1595 (C = N) cm^{-1}. Anal. Calcd. for $C_{20}H_{22}N_4O_4S$, %: C 57.96; H 5.35; N 13.52. Found: C 57.71; H 5.18; N 13.27.

2-((4-(4-Chlorophenyl)-1-(3,4,5-trimethoxyphenyl)-1 H-imidazol-2-yl)thio)acetohydrazide (**9**) White solid, yield: 2.10 g (65%) mp 198–200 °C. ^{1}H NMR (400 MHz, DMSO-d$_6$): δ 3.72 (s, 3 H, OCH$_3$), and 3.83 (s, 6 H, 2x OCH$_3$), 3.88 (s, 2 H, CH$_2$), 4.31 (br. s., 2 H, NH$_2$), 6.86 (s, 2 H, H$_{Ar}$), 7.44 and 7.83 (2t, J = 8.1 Hz, 4 H, H$_{Ar}$), 8.07 (s, 1H, NCH), 9.37 (s, 1H, NH). ^{13}C NMR (101 MHz, DMSO-d$_6$): δ 35.1 (CH$_2$), 56.3, 60.2 (3x OCH$_3$), 103.1, 119.9, 125.9, 128.6, 130.9, 132.2, 132.5, 137.3, 139.7, 141.7, 153.1 (C$_{Ar}$) 166.7 (C = O). IR (KBr): ν_{max} = 3206, 3116 (NH2, NH), 1669 (C = O), 1595 (C = N) cm^{-1}. Anal. Calcd. for $C_{20}H_{21}ClN_4O_4S$, %: C 53.51; H 4.72; N 12.48. Found: C 53.29; H 4.53; N 12.25.

General procedure for the Preparation of hydrazones 10 – 17

To a cooled solution of hydrazide **8** or **9** (0.2 g, 0.48 mmol) in propan-2-ol (10 mL), the corresponding aromatic aldehyde (0.58 mmol) was added, and the mixture was heated at reflux for 2 h[82]. Then, the mixture was cooled, and the formed solid was filtered off, washed with 2-propanol, and recrystallized from the mixture of methanol and water (2:1) to give the titles compounds **10–17**.

N’-benzylidene-2-((4-phenyl-1-(3,4,5-trimethoxyphenyl)-1 H-imidazol-2-yl)thio)acetohydrazide (**10a**) White solid, yield: 0.16 g (67%) mp 170–172 °C. ^{1}H NMR (400 MHz, DMSO-d$_6$): δ (mixture of the *Z*/*E* isomers, 60/40) 3.71, 3.81 and 3.84 (3s, 9 H, 3x OCH$_3$), 4.03 and 4.47 (2s, 2 H, CH$_2$), 6.79 – 6.90 (m, 2 H, H$_{Ar}$), 7.14 – 7.50 (m, 6 H, H$_{Ar}$), 7.58 – 7.71 (m, 2 H, H$_{Ar}$), 7.74 – 7.85 (m, 2 H, H$_{Ar}$), 7.96 – 8.27 (m, 2 H, H$_{Ar}$, N = CH, N-CH), 11.61 and 11.86 (2s, 1H, NH). ^{13}C NMR (101 MHz, DMSO-d$_6$): δ 34.8, 35.9 (CH$_2$), 56.2, 56.3, 60.2 (3x OCH$_3$), 102.9, 119.4, 124.3, 124.4, 126.7, 126.8, 127.1, 128.5, 128.8, 128.9, 129.9, 130.1, 132.4, 133.6, 134.1, 137.1, 137.2, 140.8, 141.2, 141.4, 143.4, 146.8, 153.1, 153.2, 164.2 (C$_{Ar}$) 169.6 (C = O). IR (KBr): ν_{max} = 3076 (NH), 1670 (C = O), 1593 (C = N) cm^{-1}. Anal. Calcd. for $C_{27}H_{26}N_4O_4S$, %: C 64.53; H 5.21; N 11.15. Found: C 64.34; H 5.02; N 10.92.

N’-(4-fluorobenzylidene)-2-((4-phenyl-1-(3,4,5-trimethoxyphenyl)-1 H-imidazol-2-yl)thio)acetohydrazide (**10b**) White solid, yield: 0.19 g (75%) mp 98–100 °C. ^{1}H NMR (400 MHz, DMSO-d$_6$): δ (mixture of the *Z*/*E* isomers, 60/40) 3.71, 3.81 and 3.84 (3s, 9 H, 3x OCH$_3$), 4.03 and 4.45 (2s, 2 H, CH$_2$), 6.81 – 6.89 (m, 2 H, H$_{Ar}$), 7.14 – 7.40 (m, 5 H, H$_{Ar}$), 7.66 – 7.85 (m, 4 H, H$_{Ar}$), 7.98 – 8.27 (m, 2 H, H$_{Ar}$, N = CH, N-CH), 11.62 and 11.89 (2s, 1H, NH). ^{13}C NMR (101 MHz, DMSO-d$_6$): δ 34.8, 35.9 (CH$_2$), 56.2, 56.3, 60.2 (3x OCH$_3$), 103.0, 115.7, 115.8, 115.9, 116.1, 119.5, 124.3, 124.4, 128.5, 128.9, 129.1, 129.2, 129.3, 130.7, 132.3, 137.2, 137.2, 140.7, 140.8, 141.2, 141.3, 142.3, 145.7, 153.1, 161.7, 161.9. 164.1, 164.2 (C$_{Ar}$) 169.6 (C = O). IR (KBr): ν_{max} = 3070 (NH), 1698 (C = O), 1597 (C = N) cm^{-1}. Anal. Calcd. for $C_{27}H_{25}FN_4O_4S$, %: C 62.30; H 4.84; N 10.76. Found: C 62.17; H 4.57; N 10.57.

N’-(4-chlorobenzylidene)-2-((4-phenyl-1-(3,4,5-trimethoxyphenyl)-1 H-imidazol-2-yl)thio)acetohydrazide (**10c**) White solid, yield: 0.19 g (77%) mp 168–170 °C. ^{1}H NMR (400 MHz, DMSO-d$_6$): δ (mixture of the *Z*/*E* isomers, 60/40) 3.71, 3.81 and 3.84 (3s, 9 H, 3x OCH$_3$), 4.03 and 4.45 (2s, 2 H, CH$_2$), 6.82 – 6.89 (m, 2 H, H$_{Ar}$), 7.17 – 7.54 (m, 5 H, H$_{Ar}$), 7.63 – 7.84 (m, 4 H, H$_{Ar}$), 7.98 – 8.26 (m, 2 H, H$_{Ar}$, N = CH, N-CH), 11.67 and 11.90 (2s, 1H, NH). ^{13}C NMR (101 MHz, DMSO-d$_6$): δ 34.7, 35.9 (CH$_2$), 56.2, 56.3, 60.2 (3x OCH$_3$), 102.9, 119.4, 124.3, 124.4, 126.8, 128.4, 128.5, 128.7, 128.8, 128.9, 132.4, 133.0, 133.6, 134.3, 134.5, 137.1, 140.8, 141.2, 141.3, 142.1, 145.4, 153.1, 153.2, 164.3 (C$_{Ar}$) 169.7 (C = O). IR (KBr): ν_{max} = 3255 (NH), 1699 (C = O), 1601 (C = N) cm^{-1}. Anal. Calcd. for $C_{27}H_{25}ClN_4O_4S$, %: C 60.39; H 4.69; N 10.43. Found: C 60.21; H 4.53; N 10.29.

N’-(4-bromobenzylidene)-2-((4-phenyl-1-(3,4,5-trimethoxyphenyl)-1 H-imidazol-2-yl)thio)acetohydrazide (**10d**) White solid, yield: 0.23 g (83%) mp 184–186 °C. ^{1}H NMR (400 MHz, DMSO-d$_6$): δ (mixture of the *Z*/*E* isomers, 60/40) 3.71, 3.81 and 3.84 (3s, 9 H, 3x OCH$_3$), 4.03 and 4.45 (2s, 2 H, CH$_2$), 6.81 – 6.90 (m, 2 H, H$_{Ar}$), 7.17 – 7.39 (m, 3 H, H$_{Ar}$), 7.48 – 7.85 (m, 6 H, H$_{Ar}$), 7.96 – 8.23 (m, 2 H, H$_{Ar}$, N = CH, N-CH), 11.67 and 11.93 (2s, 1H, NH). ^{13}C NMR (101 MHz, DMSO-d$_6$): δ 34.7, 35.9 (CH$_2$), 56.2, 56.3, 60.2 (3x OCH$_3$), 102.9, 119.4, 123.1, 123.4, 124.3, 124.4, 126.7, 126.8, 128.5, 128.7, 128.9, 130.2, 131.8, 131.9, 132.0, 132.3, 132.4, 133.4, 133.5, 133.6, 137.1, 137.2, 140.8, 140.9, 141.2, 141.3, 142.2, 145.5, 153.1, 153.2, 164.3 (C$_{Ar}$) 169.7 (C = O). IR (KBr): ν_{max} = 3242 (NH), 1698 (C = O), 1603 (C = N) cm^{-1}. Anal. Calcd. for $C_{27}H_{25}BrN_4O_4S$, %: C 55.77; H 4.33; N 9.64. Found: C 55.54; H 4.30; N 9.57.

N'-(4-(dimethylamino)benzylidene)-2-((4-phenyl-1-(3,4,5-trimethoxyphenyl)-1H-imidazol-2-yl)thio)acetohydrazide (**10e**) Light orange solid, yield: 0.21 g (82%) mp 208–210 °C. ^{1}H NMR (400 MHz, DMSO-d$_6$): δ (mixture of the *Z*/*E* isomers, 60/40) 2.93 and 2.95 (2s, 6 H, 2x CH$_3$), 3.71, 3.81 and 3.84 (3s, 9 H, 3x OCH$_3$), 3.99 and 4.42 (2s, 2 H, CH$_2$), 6.56 – 6.89 (m, 4 H, H$_{Ar}$), 7.13 – 7.51 (m, 5 H, H$_{Ar}$), 7.71 – 8.08 (m, 4 H, H$_{Ar}$, N = CH, N-CH), 11.32 and 11.54 (2s, 1H, NH). ^{13}C NMR (101 MHz, DMSO-d$_6$): δ 30.4, 30.8 (2x CH$_3$), 35.0, 36.0 (CH$_2$), 56.2, 56.3, 60.2 (3x OCH$_3$), 103.0, 111.7, 111.8, 119.4, 121.3, 121.4, 124.3, 124.4, 126.7, 126.8, 128.1, 128.4, 128.5, 132.4, 133.6, 133.7, 137.1, 137.2, 140.8, 141.3, 141.6, 144.2, 147.6, 151.3, 151.5, 153.1, 153.2, 163.5 (C$_{Ar}$) 169.9 (C = O). IR (KBr): ν_{max} = 3246 (NH), 1689 (C = O), 1600 (C = N) cm^{-1}. Anal. Calcd. for $C_{29}H_{31}N_5O_4S$, %: C 63.83; H 5.73; N 12.83. Found: C 63.75; H 5.47; N 12.78.

N'-(4-nitrobenzylidene)-2-((4-phenyl-1-(3,4,5-trimethoxyphenyl)-1H-imidazol-2-yl)thio)acetohydrazide (**10f**) Yellow solid, yield: 0.23 g (87%) mp 242–244 °C. ^{1}H NMR (400 MHz, DMSO-d$_6$): δ (mixture of the *Z*/*E* isomers, 60/40) 3.71, 3.82 and 3.84 (3s, 9 H, 3x OCH$_3$), 4.07 and 4.47 (2s, 2 H, CH$_2$), 6.63 – 6.96 (m, 2 H, H$_{Ar}$), 7.04 – 7.46 (m, 3 H, H$_{Ar}$), 7.60 – 8.42 (m, 8 H, H$_{Ar}$, N = CH, N-CH), 11.90 and 12.16 (2s, 1H, NH). ^{13}C NMR (101 MHz, DMSO-d$_6$): δ 34.6, 35.9 (CH$_2$), 56.2, 56.3, 60.2 (3x OCH$_3$), 102.9, 119.5, 123.9, 124.1, 124.3, 124.4, 126.7, 127.7, 128.0, 128.5, 132.4, 133.6, 137.1, 140.4, 140.5, 140.8, 140.9, 141.1, 144.2, 147.7, 147.9, 153.1, 153.2, 164.7 (C$_{Ar}$) 170.1 (C = O). IR (KBr): ν_{max} = 3240 (NH), 1708 (C = O), 1600 (C = N) cm^{-1}. Anal. Calcd. for $C_{27}H_{25}N_5O_6S$, %: C 59.22; H 4.60; N 12.79. Found: C 59.19; H 4.53; N 12.68.

N'-benzylidene-2-((4-(4-chlorophenyl)-1-(3,4,5-trimethoxyphenyl)-1H-imidazol-2-yl)thio)acetohydrazide (**11a**) White solid, yield: 0.23 g (90%) mp 222–224 °C. ^{1}H NMR (400 MHz, DMSO-d$_6$): δ (mixture of the *Z*/*E* isomers, 60/40) 3.71, 3.81 and 3.83 (3s, 9 H, 3x OCH$_3$), 4.03 and 4.46 (2s, 2 H, CH$_2$), 6.80 – 6.89 (m, 2 H, H$_{Ar}$), 7.29 – 7.48 (m, 5 H, H$_{Ar}$), 7.62 – 7.71 (m, 2 H, H$_{Ar}$), 7.76 – 7.87 (m, 2 H, H$_{Ar}$), 7.97 – 8.25 (m, 2 H, H$_{Ar}$, N = CH, N-CH), 11.60 and 11.79 (2s, 1H, NH). ^{13}C NMR (101 MHz, DMSO-d$_6$): δ 34.8, 35.9 (CH$_2$), 56.2, 56.3, 60.2 (3x OCH$_3$), 103.0, 119.9, 125.9, 126.0, 126.9, 127.1, 128.5, 128.8, 128.9, 130.0, 130.2, 130.9, 131.0, 132.2, 132.3, 132.6, 134.1, 137.2, 139.6, 139.7, 141.6, 141.9, 143.4, 146.8, 153.1, 153.2, 164.1 (C$_{Ar}$) 169.5 (C = O). IR (KBr): ν_{max} = 3079 (NH), 1676 (C = O), 1595 (C = N) cm^{-1}. Anal. Calcd. for $C_{27}H_{25}ClN_4O_4S$, %: C 60.39; H 4.69; N 10.43. Found: C 60.29; H 4.57; N 10.36.

2-((4-(4-chlorophenyl)-1-(3,4,5-trimethoxyphenyl)-1H-imidazol-2-yl)thio)-N'-(4-fluorobenzylidene)acetohydrazide (**11b**) White solid, yield: 0.24 g (88%) mp 176–178 °C. ^{1}H NMR (400 MHz, DMSO-d$_6$): δ (mixture of the *Z*/*E* isomers, 60/40) 3.71, 3.81 and 3.83 (3s, 9 H, 3x OCH$_3$), 4.03 and 4.45 (2s, 2 H, CH$_2$), 6.74 – 6.92 (m, 2 H, H$_{Ar}$), 7.12 – 7.48 (m, 4 H, H$_{Ar}$), 7.60 – 7.89 (m, 4 H, H$_{Ar}$), 7.96 – 8.27 (m, 2 H, H$_{Ar}$, N = CH, N-CH), 11.62 and 11.83 (2s, 1H, NH). ^{13}C NMR (101 MHz, DMSO-d$_6$): δ 34.8, 35.9 (CH$_2$), 56.2, 56.3, 60.2 (3x OCH$_3$), 103.0, 115.7, 115.8, 115.9, 116.0, 119.9, 125.9, 126.0, 128.5, 128.9, 129.1, 129.2, 129.3, 130.7, 130.9, 132.2, 132.3, 132.5, 137.2, 139.7, 141.8, 142.3, 145.7, 153.1, 153.2, 164.1 (C$_{Ar}$) 169.5 (C = O). IR (KBr): ν_{max} = 3077 (NH), 1682 (C = O), 1601 (C = N) cm^{-1}. Anal. Calcd. for $C_{27}H_{24}FN_4O_4S$, %: C 58.43; H 4.36; N 10.09. Found: C 58.39; H 4.33; N 9.97.

N'-(4-chlorobenzylidene)-2-((4-(4-chlorophenyl)-1-(3,4,5-trimethoxyphenyl)-1H-imidazol-2-yl)thio)acetohydrazide (**11c**) White solid, yield: 0.18 g (68%) mp 200–202 °C. ^{1}H NMR (400 MHz, DMSO-d$_6$): δ (mixture of the *Z*/*E* isomers, 60/40) 3.71, 3.81 and 3.83 (3s, 9 H, 3x OCH$_3$), 4.03 and 4.44 (2s, 2 H, CH$_2$), 6.78 – 6.89 (m, 2 H, H$_{Ar}$), 7.31 – 7.53 (m, 4 H, H$_{Ar}$), 7.63 – 7.87 (m, 4 H, H$_{Ar}$), 7.97 – 8.23 (m, 2 H, H$_{Ar}$, N = CH, N-CH), 11.65 and 11.85 (2s, 1H, NH). ^{13}C NMR (101 MHz, DMSO-d$_6$): δ 34.8, 35.9 (CH$_2$), 56.2, 56.3, 60.2 (3x OCH$_3$), 103.0, 119.9, 125.9, 128.5, 128.6, 128.8, 128.9, 129.0, 130.9, 132.3, 132.6, 133.0, 133.1, 134.3, 137.2, 139.7, 141.6, 141.7, 142.2, 145.5, 153.1, 153.2, 164.3, 165.4 (C$_{Ar}$) 169.6 (C = O). IR (KBr): ν_{max} = 3078 (NH), 1681 (C = O), 1596 (C = N) cm^{-1}. Anal. Calcd. for $C_{27}H_{24}Cl_2N_4O_4S$, %: C 56.75; H 4.23; N 9.80. Found: C 56.68; H 4.21; N 9.76.

N'-(4-bromobenzylidene)-2-((4-(4-chlorophenyl)-1-(3,4,5-trimethoxyphenyl)-1H-imidazol-2-yl)thio)acetohydrazide (**11d**) White solid, yield: 0.27 g (89%) mp 206–208 °C. ^{1}H NMR (400 MHz, DMSO-d$_6$): δ (mixture of the *Z*/*E* isomers, 60/40) 3.71, 3.81 and 3.83 (3s, 9 H, 3x OCH$_3$), 4.03 and 4.44 (2s, 2 H, CH$_2$), 6.79 – 6.89 (m, 2 H, H$_{Ar}$), 7.29 – 7.69 (m, 6 H, H$_{Ar}$), 7.76 – 7.89 (m, 2 H, H$_{Ar}$), 7.95 – 8.22 (m, 2 H, H$_{Ar}$, N = CH, N-CH), 11.66 and 11.87 (2s, 1H, NH). ^{13}C NMR (101 MHz, DMSO-d$_6$): δ 34.7, 35.9 (CH$_2$), 56.2, 56.3, 60.2 (3x OCH$_3$), 103.0, 119.9, 123.1, 123.4, 125.9, 126.0, 128.5, 128.7, 128.9, 130.9, 131.0, 131.8, 131.9, 132.2, 132.3, 132.5, 133.3, 133.4, 137.2, 137.3, 139.7, 141.5, 141.7, 142.2, 145.6, 153.1, 153.2, 164.2 (C$_{Ar}$) 169.6 (C = O). IR (KBr): ν_{max} = 3077 (NH), 1677 (C = O), 1596 (C = N) cm^{-1}. Anal. Calcd. for $C_{27}H_{24}BrClN_4O_4S$, %: C 52.65; H 3.93; N 9.10. Found: C 52.61; H 3.87; N 8.95.

2-((4-(4-chlorophenyl)-1-(3,4,5-trimethoxyphenyl)-1H-imidazol-2-yl)thio)-N'-(4-(dimethylamino)benzylidene)acetohydrazide (**11e**) Yellowish solid, yield: 0.25 g (88%) mp 218–220 °C. ^{1}H NMR (400 MHz, DMSO-d$_6$): δ (mixture of the *Z*/*E* isomers, 60/40) 2.93 and 2.95 (2s, 6 H, 2x CH$_3$), 3.71, 3.81 and 3.83 (3s, 9 H, 3x OCH$_3$), 3.99 and 4.41 (2s, 2 H, CH$_2$), 6.58 – 6.89 (m, 4 H, H$_{Ar}$), 7.32 – 7.51 (m, 4 H, H$_{Ar}$), 7.79 – 8.09 (m, 4 H, H$_{Ar}$, N = CH, N-CH), 11.31 and 11.48 (2s, 1H, NH). ^{13}C NMR (101 MHz, DMSO-d$_6$): δ 34.9, 35.9 (CH$_2$), 56.2, 56.3, 60.2 (3x OCH$_3$), 103.0, 111.7, 111.8, 119.9, 121.3, 121.4, 125.9, 128.1, 128.4, 128.6, 130.9, 132.2, 132.3, 132.5, 132.6, 137.2, 137.3, 139.7, 141.7, 141.9, 144.2, 147.7, 151.4, 151.6, 153.1, 153.2, 163.4 (C$_{Ar}$) 168.9 (C = O).

IR (KBr): ν_{max} = 3077 (NH), 1671 (C = O), 1595 (C = N) cm^{-1}. Anal. Calcd. for $C_{29}H_{30}ClN_5O_4S$, %: C 60.04; H 5.21; N 12.07. Found: C 59.95; H 5.03; N 11.87.

2-((4-(4-chlorophenyl)-1-(3,4,5-trimethoxyphenyl)-1H-imidazol-2-yl)thio)-N'-(4-nitrobenzylidene)acetohydrazide (**11f**) Yellow solid, yield: 0.25 g (88%) mp 205–206 °C. ^1H NMR (400 MHz, DMSO-d_6): δ (mixture of the *Z*/*E* isomers, 60/40) 3.71, 3.82 and 3.84 (3s, 9 H, 3x OCH_3), 4.07 and 4.46 (2s, 2 H, CH_2), 6.74 – 6.90 (m, 2 H, H_{Ar}), 7.19 – 7.45 (m, 2 H, H_{Ar}), 7.65 – 8.38 (m, 8 H, H_{Ar}, N = CH, N-CH), 11.89 and 12.12 (2s, 1H, NH). ^{13}C NMR (101 MHz, DMSO-d_6): δ 34.7, 35.9 (CH_2), 56.2, 56.3, 60.2 (3x OCH_3), 103.0, 120.0, 123.9, 124.1, 125.9, 126.0, 127.7, 128.0, 128.5, 131.0, 132.1, 132.2, 132.5, 137.2, 137.3, 139.7, 140.3, 141.1, 141.5, 144.3, 147.7, 147.9, 153.1, 153.2, 164.7 (C_{Ar}) 169.9 (C = O). IR (KBr): ν_{max} = 3075 (NH), 1675 (C = O), 1592 (C = N) cm^{-1}. Anal. Calcd. for $C_{27}H_{24}ClN_5O_6S$, %: C 55.72; H 4.16; N 12.03. Found: C 55.38; H 3.90; N 11.87.

2-((4-phenyl-1-(3,4,5-trimethoxyphenyl)-1H-imidazol-2-yl)thio)-N'-(thien-2-ylmethylene)acetohydrazide (**12a**) Yellowish solid, yield: 0.13 g (54%) mp 160–162 °C. ^1H NMR (400 MHz, DMSO-d_6): δ (mixture of the *Z*/*E* isomers, 60/40) 3.72, 3.83 and 3.84 (3s, 9 H, 3x OCH_3), 4.00 and 4.42 (2s, 2 H, CH_2), 6.76 – 6.92 (m, 2 H, H_{Ar}), 7.01 – 7.50 (m, 5 H, H_{Ar}), 7.57 – 7.86 (m, 3 H, H_{Ar}), 7.95 – 8.49 (m, 2 H, H_{Ar}, N = CH), 11.59 and 11.78 (2s, 1H, NH). ^{13}C NMR (101 MHz, DMSO-d_6): δ 34.7, 35.9 (CH_2), 56.2, 56.3, 60.2 (3x OCH_3), 102.9, 103.0, 119.3, 119.4, 124.3, 124.4, 126.7, 127.9, 128.5, 129.0, 130.5, 131.1, 132.3, 132.4, 133.5, 137.1, 138.6, 138.8, 140.8, 140.9, 141.1, 141.5, 141.9, 153.1, 153.2, 164.0 (C_{Ar}) 169.1 (C = O). IR (KBr): ν_{max} = 3087 (NH), 1660 (C = O), 1594 (C = N) cm^{-1}. Anal. Calcd. for $C_{25}H_{24}N_4O_4S_2$, %: C 59.04; H 4.76; N 11.02. Found: C 58.89; H 4.68; N 10.96.

N'-((5-nitrothien-2-yl)methylene)-2-((4-phenyl-1-(3,4,5-trimethoxyphenyl)-1H-imidazol-2-yl)thio)acetohydrazide (**12b**) Yellow solid, yield: 0.21 g (78%) mp 226–228 °C. ^1H NMR (400 MHz, DMSO-d_6): δ (mixture of the *Z*/*E* isomers, 60/40) 3.72, 3.83 and 3.84 (3s, 9 H, 3x OCH_3), 4.05 and 4.44 (2s, 2 H, CH_2), 6.86 (s, 2 H, H_{Ar}), 7.13 – 7.39 (m, 3 H, H_{Ar}), 7.48 – 7.60 (m, 1H, H_{Ar}), 7.73 – 7.83 (m, 2 H, H_{Ar}), 7.93 – 8.55 (m, 3 H, H_{Ar}, N = CH), 12.03 and 12.22 (2s, 1H, NH). ^{13}C NMR (101 MHz, DMSO-d_6): δ 34.6, 35.8 (CH_2), 56.2, 56.3, 60.2 (3x OCH_3), 102.9, 119.4, 124.2, 124.3, 126.7, 128.4, 129.3, 129.8, 130.5, 130.6, 132.2, 133.6, 136.7, 137.1, 137.2, 140.2, 140.8, 140.9, 141.1, 146.5, 150.5, 150.8, 153.1, 153.2, 164.8 (C_{Ar}) 169.8 (C = O). IR (KBr): ν_{max} = 3248 (NH), 1702 (C = O), 1592 (C = N) cm^{-1}. Anal. Calcd. for $C_{25}H_{23}N_5O_6S_2$, %: C 54.24; H 4.19; N 12.65. Found: C 54.20; H 3.99; N 12.38.

2-((4-(4-chlorophenyl)-1-(3,4,5-trimethoxyphenyl)-1H-imidazol-2-yl)thio)-N'-(thien-2-ylmethylene)acetohydrazide (**13a**) White solid, yield: 0.23 g (89%) mp 206–208 °C. ^1H NMR (400 MHz, DMSO-d_6): δ (mixture of the *Z*/*E* isomers, 60/40) 3.71, 3.82 and 3.83 (3s, 9 H, 3x OCH_3), 4.00 and 4.41 (2s, 2 H, CH_2), 6.81 – 6.90 (m, 2 H, H_{Ar}), 7.09 – 7.16 (m, 1H, H_{Ar}), 7.30 – 7.69 (m, 4 H, H_{Ar}), 7.75 – 7.90 (m, 2 H, H_{Ar}), 7.98 – 8.50 (m, 2 H, H_{Ar}, N = CH), 11.58 and 11.74 (2s, 1H, NH). ^{13}C NMR (101 MHz, DMSO-d_6): δ 34.6, 35.9 (CH_2), 56.2, 56.3, 60.2 (3x OCH_3), 102.9, 103.0, 119.8, 119.9, 125.9, 126.0, 127.9, 128.5, 128.6, 129.1, 130.6, 130.9, 131.0, 131.1, 132.2, 132.3, 132.5, 132.6, 137.2, 137.3, 138.6, 138.8, 139.6, 139.8, 141.6, 141.9, 142.0, 153.1, 153.2, 164.0 (C_{Ar}) 169.1 (C = O). IR (KBr): ν_{max} = 3202 (NH), 1654 (C = O), 1595 (C = N) cm^{-1}. Anal. Calcd. for $C_{25}H_{23}ClN_4O_4S_2$, %: C 55.29; H 4.27; N 10.32. Found: C 55.25; H 4.21; N 10.27.

2-((4-(4-chlorophenyl)-1-(3,4,5-trimethoxyphenyl)-1H-imidazol-2-yl)thio)-N'-((5-nitrothien-2-yl)methylene)acetohydrazide (**13b**) Orange solid, yield: 0.25 g (88%) mp 206–208 °C. ^1H NMR (400 MHz, DMSO-d_6): δ (mixture of the *Z*/*E* isomers, 60/40) 3.71, 3.83 and 3.84 (3s, 9 H, 3x OCH_3), 4.04 and 4.42 (2s, 2 H, CH_2), 6.86 (s, 2 H, H_{Ar}), 7.34 – 7.45 (m, 2 H, H_{Ar}), 7.47 – 7.63 (m, 1H, H_{Ar}), 7.72 – 7.85 (m, 2 H, H_{Ar}), 8.01 – 8.51 (m, 3 H, H_{Ar}, N = CH), 12.01 and 12.16 (2s, 1H, NH). ^{13}C NMR (101 MHz, DMSO-d_6): δ 34.6, 35.8 (CH_2), 56.2, 56.3, 60.2 (3x OCH_3), 102.9, 119.9, 125.8, 125.9, 128.5, 128.6, 129.3, 129.9, 130.5, 130.6, 130.9, 132.1, 132.2, 132.4, 132.5, 136.8, 137.3, 139.7, 139.8, 140.3, 141.4, 141.6, 146.5, 150.6, 150.9, 153.1, 153.2, 164.7 (C_{Ar}) 169.8 (C = O). IR (KBr): ν_{max} = 3123 (NH), 1672 (C = O), 1583 (C = N) cm^{-1}. Anal. Calcd. for $C_{25}H_{22}ClN_5O_6S_2$, %: C 51.06; H 3.77; N 11.91. Found: C 50.78; H 3.47; N 11.77.

N'-(naphthalen-1-ylmethylene)-2-((4-phenyl-1-(3,4,5-trimethoxyphenyl)-1H-imidazol-2-yl)thio)acetohydrazide (**14**) White solid, yield: 0.22 g (81%) mp 184–186 °C. ^1H NMR (400 MHz, DMSO-d_6): δ (mixture of the *Z*/*E* isomers, 60/40) 3.70, 3.72, 3.81 and 3.84 (4s, 9 H, 3x OCH_3), 4.09 and 4.59 (2s, 2 H, CH_2), 6.77 – 6.95 (m, 2 H, H_{Ar}), 7.13 – 8.11 (m, 12 H, H_{Ar}), 8.60 – 8.92 (m, 2 H, H_{Ar}, N = CH), 11.70 and 12.01 (2s, 1H, NH). ^{13}C NMR (101 MHz, DMSO-d_6): δ 35.2, 35.8 (CH_2), 56.2, 56.3, 60.2 (3x OCH_3), 102.9, 119.3, 123.8, 124.3, 124.4, 125.6, 126.3, 126.7, 126.8, 127.3, 127.4, 127.9, 128.4, 128.5, 128.9, 129.3, 130.1, 130.4, 130.7, 132.4, 133.6, 137.1, 140.8, 141.3, 141.5, 143.4, 146.6, 153.1, 153.2, 164.3 (C_{Ar}) 169.4 (C = O). IR (KBr): ν_{max} = 3144 (NH), 1670 (C = O), 1599 (C = N) cm^{-1}. Anal. Calcd. for $C_{31}H_{28}N_4O_4S$, %: C 67.37; H 5.11; N 10.14. Found: C 67.17; H 4.87; N 9.87.

2-((4-(4-chlorophenyl)-1-(3,4,5-trimethoxyphenyl)-1H-imidazol-2-yl)thio)-N'-(naphthalen-1-ylmethylene)acetohydrazide (**15**) White solid, yield: 0.23 g (81%) mp 202–204 °C. ^1H NMR (400 MHz, DMSO-d_6): δ (mixture of the *Z*/*E* isomers, 60/40) 3.70, 3.72, 3.81 and 3.84 (4s, 9 H, 3x OCH_3), 4.09 and 4.57 (2s, 2 H, CH_2), 6.83 – 6.93 (m, 2 H, H_{Ar}), 7.25 – 8.11 (m, 11 H, H_{Ar}), 8.61 – 8.90 (m, 2 H, H_{Ar}, N = CH), 11.68 and 11.93 (2s, 1H, NH). ^{13}C NMR (101 MHz, DMSO-d_6): δ 35.3, 35.9 (CH_2), 56.4, 56.5, 60.4 (3x OCH_3), 103.2, 120.0, 120.1, 124.0, 124.3, 125.8, 126.1, 126.2, 126.4, 126.5, 127.5, 128.1, 128.7, 128.8, 129.0, 129.1, 129.4, 129.5, 130.2, 130.3, 130.6, 130.9, 131.1, 131.2, 132.3, 132.4, 132.7, 133.7, 133.8, 137.4, 137.5, 139.8, 139.9, 141.9, 142.1, 143.5, 146.9, 153.3, 153.4, 164.4 (C_{Ar}) 169.6 (C = O). IR (KBr): ν_{max} = 3082 (NH), 1681 (C = O), 1596 (C = N) cm^{-1}. Anal. Calcd. for $C_{31}H_{27}ClN_4O_4S$, %: C 63.42; H 4.64; N 9.54. Found: C 63.21; H 4.35; N 9.19.

N’-(naphthalen-2-ylmethylene)-2-((4-phenyl-1-(3,4,5-trimethoxyphenyl)-1 H-imidazol-2-yl)thio)acetohydrazide (**16**) Yellowish solid, yield: 0.21 g (80%) mp 178–180 °C. ^{1}H NMR (400 MHz, DMSO-d$_6$): δ (mixture of the *Z*/*E* isomers, 60/40) 3.70, 3.72, 3.81 and 3.85 (4s, 9 H, 3x OCH_3), 4.07 and 4.54 (2s, 2 H, CH_2), 6.82 – 6.90 (m, 2 H, H_{Ar}), 7.13 – 7.41 (m, 3 H, H_{Ar}), 7.49 – 7.67 (m, 2 H, H_{Ar}), 7.75 – 8.44 (m, 9 H, H_{Ar}, N = CH), 11.71 and 11.95 (2s, 1H, NH). ^{13}C NMR (101 MHz, DMSO-d$_6$): δ 34.9, 35.9 (CH_2), 56.2, 56.3, 60.2 (3x OCH_3), 103.0, 119.4, 122.3, 122.6, 124.3, 124.4, 126.7, 126.8, 127.1, 127.8, 128.3, 128.4, 128.5, 128.7, 128.8, 131.8, 131.9, 132.3, 132.4, 132.9, 133.5, 133.6, 133.7, 137.1, 137.2, 140.8, 140.9, 141.2, 141.5, 143.5, 146.7, 153.1, 153.2, 164.2 (C_{Ar}) 169.6 (C = O). IR (KBr): ν_{max} = 3059 (NH), 1668 (C = O), 1598 (C = N) cm^{-1}. Anal. Calcd. for $C_{31}H_{28}N_4O_4S$, %: C 67.37; H 5.11; N 10.14. Found: C 67.35; H 5.05; N 10.11.

2-((4-(4-chlorophenyl)-1-(3,4,5-trimethoxyphenyl)-1 H-imidazol-2-yl)thio)-N’-(naphthalen-2-ylmethylene) acetohydrazide (**17**) White solid, yield: 0.21 g (74%) mp 220–222 °C. ^{1}H NMR (400 MHz, DMSO-d$_6$): δ (mixture of the *Z*/*E* isomers, 60/40) 3.71, 3.72, 3.81 and 3.84 (4s, 9 H, 3x OCH_3), 4.07 and 4.52 (2s, 2 H, CH_2), 6.83 – 6.91 (m, 2 H, H_{Ar}), 7.29 – 8.13 (m, 12 H, H_{Ar}), 8.14 – 8.41 (m, 2 H, N = CH), 11.78 (br. s, 1H, NH). ^{13}C NMR (101 MHz, DMSO-d$_6$): δ 34.9, 35.9 (CH_2), 56.2, 56.3, 60.2 (3x OCH_3), 103.0, 119.4, 122.3, 122.6, 124.3, 124.4, 126.7, 126.8, 127.1, 127.8, 128.3, 128.4, 128.5, 128.7, 128.8, 131.8, 131.9, 132.3, 132.4, 132.9, 133.5, 133.6, 133.7, 137.1, 137.2, 140.8, 140.9, 141.2, 141.5, 143.5, 146.7, 153.1, 153.2, 164.2 (C_{Ar}) 169.6 (C = O). IR (KBr): ν_{max} = 3058 (NH), 1676 (C = O), 1594 (C = N) cm^{-1}. Anal. Calcd. for $C_{31}H_{27}ClN_4O_4S$, %: C 63.42; H 4.64; N 9.54. Found: C 63.39; H 4.60; N 9.49.

General procedure for the Preparation of pyrazoles 18, 19

To a cooled solution of hydrazides **8** or **9** (0.72 mmol) in propan-2-ol (15 mL), pentane-2,4-dione (0.11 g, 1.08 mmol) and a catalytic amount of concentrated hydrochloric acid (3 drops) were added, and the mixture was heated at reflux for 2 h[82]. When completed, the mixture was cooled, and the obtained crystalline solid was filtered off, washed with propan-2-ol, and recrystallized from 1,4-dioxane to give the titles compounds **18** and **19**.

1-(3,5-dimethyl-1 H-pyrazol-1-yl)-2-((4-phenyl-1-(3,4,5-trimethoxyphenyl)-1 H-imidazol-2-yl)thio)ethan-1-one (**18**) White solid, yield: 0.31 g (90%) mp 100–102 °C. ^{1}H NMR (400 MHz, DMSO-d$_6$): δ 1.17 and 1.19 (2s, 6 H, CH_3), 3.72, 3.82 and 3.84 (3s, 9 H, 3x OCH_3), 4.01 (s, 2 H, CH_2), 4.93 (p, *J* = 6.5 Hz, 1H, C*H*CCH$_3$), 6.86 (s, 2 H, H_{Ar}), 7.23 (t, *J* = 7.4 Hz, 1H, H_{Ar}), 7.37 (t, *J* = 7.4 Hz, 2 H, H_{Ar}), 7.71 – 7.78 (m, 2 H, H_{Ar}), 8.01 (m, 1H, N = CH). ^{13}C NMR (101 MHz, DMSO-d$_6$): δ 21.4 (2x CH_3), 35.0 (CH_2), 56.3, 60.2, 68.9 (3x OCH_3), 102.8, 119.2, 124.4, 126.8, 128.5, 132.2, 133.5, 137.2, 140.8, 141.0, 153.1, 153.2 (C_{Ar}) 168.2 (C = O). IR (KBr): ν_{max} = 1733 (C = O), 1594 (C = N) cm^{-1}. Anal. Calcd. for $C_{25}H_{26}N_4O_4S$, %: C 62.74; H 5.48; N 11.71. Found: C 62.63; H 5.36; N 11.65.

2-((4-(4-chlorophenyl)-1-(3,4,5-trimethoxyphenyl)-1 H-imidazol-2-yl)thio)-1-(3,5-dimethyl-1 H-pyrazol-1-yl)ethan-1-one (**19**) White solid, yield: 0.35 g (87%) mp 246–248 °C. ^{1}H NMR (400 MHz, DMSO-d$_6$): δ 1.18 and 1.20 (2s, 6 H, CH_3), 3.71 (s, 3 H, OCH_3) and 3.81 (s, 6 H, 2x OCH_3), 4.02 (s, 2 H, CH_2), 4.90 (p, *J* = 6.5 Hz, 1H, C*H*CCH$_3$), 6.86 (s, 2 H, H_{Ar}), 7.41 (t, *J* = 7.4 Hz, 2 H, H_{Ar}), 7.84 (t, *J* = 7.4 Hz, 2 H, H_{Ar}), 8.06 (s, 1H, N = CH). ^{13}C NMR (101 MHz, DMSO-d$_6$): δ 21.5 (2x CH_3), 34.9 (CH_2), 56.3, 60.2, 68.3 (3x OCH_3), 103.1, 119.9, 126.1, 128.5, 131.1, 132.1, 132.3, 137.3, 139.6, 141.6, 153.2 (C_{Ar}) 165.9 (C = O). IR (KBr): ν_{max} = 1731 (C = O), 1598 (C = N) cm^{-1}. Anal. Calcd. for $C_{25}H_{25}ClN_4O_4S$, %: C 58.53; H 4.91; N 10.92. Found: C 58.27; H 4.65; N 10.63.

General procedure for the Preparation of pyroles 20, 21

To a solution of hydrazide **8** or **9** (0.72 mmol) in propan-2-ol (15 mL), hexane-2,5-dione (0.16 g, 1.44 mmol) and glacial acetic acid (3 drops) were added dropwise, and the mixture was heated at reflux for 3 h[82]. Then, the reaction mixture was cooled, and the formed crystalline solid was filtered off, washed with propan-2-ol, and recrystallized from 1,4-dioxane to give the titles compounds **20** and **21**.

N-(2,5-dimethyl-1 H-pyrrol-1-yl)-2-((4-phenyl-1-(3,4,5-trimethoxyphenyl)-1 H-imidazol-2-yl)thio)acetamide (**20**) White solid, yield: 0.30 g (86%) mp 122–124 °C. ^{1}H NMR (400 MHz, DMSO-d$_6$): δ 1.89 (s, 6 H, CH_3), 3.73 (s, 3 H, OCH_3), and 3.84 (s, 6 H, 2x OCH_3), 4.11 (s, 2 H, CH_2), 5.59 (s, 2 H, H_{Pyrr}), 6.89 (s, 2 H, H_{Ar}), 7.24 (t, *J* = 7.4 Hz, 1H, H_{Ar}), 7.38 (t, *J* = 7.4 Hz, 2 H, H_{Ar}), 7.85 (d, *J* = 7.6 Hz, 2 H, H_{Ar}), 8.03 (s, 1H, N = CH), 10.95 (s, 1H, NH). ^{13}C NMR (101 MHz, DMSO-d$_6$): δ 10.9 (2x CH_3), 34.5 (CH_2), 56.3, 60.2 (2x OCH_3), 102.9, 103.0, 119.4, 124.4, 126.7, 126.9, 128.4, 132.2, 133.5, 137.2, 140.9, 141.0, 153.2 (C_{Ar}) 167.2 (C = O). IR (KBr): ν_{max} = 3264 (NH), 1670 (C = O), 1598 (C = N) cm^{-1}. Anal. Calcd. for $C_{26}H_{28}N_4O_4S$, %: C 63.40; H 5.73; N 11.37. Found: C 63.31; H 5.53; N 11.27.

2-((4-(4-chlorophenyl)-1-(3,4,5-trimethoxyphenyl)-1 H-imidazol-2-yl)thio)-N-(2,5-dimethyl-1 H-pyrrol-1-yl) acetamide (**21**) Light orange solid, yield: 0.25 g (67%) mp 172–174 °C. ^{1}H NMR (400 MHz, DMSO-d$_6$): δ 1.88 (s, 6 H, CH_3), 3.72 (s, 3 H, OCH_3), and 3.83 (s, 6 H, 2x OCH_3), 4.13 (s, 2 H, CH_2), 5.58 (s, 2 H, H_{Pyrr}), 6.89 (s, 2 H, H_{Ar}), 7.44 (d, *J* = 8.7 Hz, 2 H, H_{Ar}), 7.87 (t, *J* = 8.7 Hz, 2 H, H_{Ar}), 8.11 (s, 1H, N = CH), 10.99 (s, 1H, NH). ^{13}C NMR (101 MHz, DMSO-d$_6$): δ 10.9 (2x CH_3), 34.5 (CH_2), 56.3, 60.2 (2x OCH_3), 102.9, 103.0, 119.9, 126.0, 126.8, 128.5, 131.0, 132.1, 132.5, 137.2, 139.8, 141.2, 153.2 (C_{Ar}) 167.2 (C = O). IR (KBr): ν_{max} = 3243 (NH), 1684 (C = O), 1597 (C = N) cm^{-1}. Anal. Calcd. for $C_{26}H_{27}ClN_4O_4S$, %: C 59.25; H 5.16; N 10.63. Found: C 59.07; H 4.87; N 10.36.

Physicochemical properties and drug-likeness analysis

In silico evaluation of physicochemical properties and drug-likeness was performed for all synthesized thioimidazole–TMP conjugates using the SwissADME web-based platform[76]. Chemical structures were entered as SMILES strings, and default calculation settings were applied. The analysis included determination of MW, HBD, HBA, lipophilicity expressed as consensus logP, TPSA, NRB, predicted aqueous solubility class, and bioavailability score. Drug-likeness was assessed according to Lipinski's Rule of Five and Veber's criteria, which are commonly used filters at early stages of small-molecule drug discovery[77–79]. Predicted solubility and bioavailability scores were obtained directly from the SwissADME output.

Data availability

The data that support the findings of this study are available from the corresponding authors, Dr Natalia Maciejewska and Dr Birutė Grybaitė, upon reasonable request.

Received: 4 November 2025; Accepted: 17 January 2026

References

1. Tolomeu, H. V. & Fraga, C. A. M. Imidazole synthesis, functionalization and physicochemical properties of a privileged structure in medicinal chemistry. *Molecules* **28**, 838 (2023).
2. Verma, A., Joshi, S. & Singh, D. Imidazole: having versatile biological activities. *J. Chem.* **2013** (329412). https://doi.org/10.3390/molecules28020838 (2013).
3. Zhang, X. et al. Insight into the stabilization mechanism of imidazole-based ionic liquids at the interface of the carbon nanotubes: A computational study. *J. Mol. Liq.* **375**, 121320. https://doi.org/10.1016/j.molliq.2023.121320 (2023).
4. Gujjarappa, R. et al. Overview on biological activities of imidazole derivatives. In *Materials Horizons: from Nature To Nanomaterials*, Vol. 1, no. 6, 135–227. (Springer, 2022). https://doi.org/10.1007/978-981-16-8399-2_6.
5. Mahdy, A. R. E. et al. Synthesis, characterization, and biological activity of Co(II) and Zn(II) complexes of imidazoles-based azo-functionalized schiff bases. *J. Mol. Struct.* **1259**, 132726. https://doi.org/10.1016/j.molstruc.2022.132726 (2022).
6. Romero, D. H., Heredia, V. E. T., García-Barradas, O., López, Ma, E. M. & Pavón, E. S. Synthesis of imidazole derivatives and their biological activities. *JCB* 2 https://doi.org/10.15640/JCB.V2N2A3 (2014).
7. Muheyuddeen, G. et al. Design, synthesis, and biological evaluation of novel imidazole derivatives as analgesic and anti-inflammatory agents: experimental and molecular Docking insights. *Sci. Rep.* **14** (23121). https://doi.org/10.1038/s41598-024-72399-8 (2024).
8. Puratchikody, A. & Doble, M. Antinociceptive and antiinflammatory activities and QSAR studies on 2-substituted-4,5-diphenyl-1H-imidazoles. *Bioorg. Med. Chem.* **15**, 1083–1090. https://doi.org/10.1007/s00706-018-2167-1 (2007).
9. Ghorbani-Vaghei, R., Izadkhah, V., Mahmoodi, J., Karamian, R. & Ahmadi Khoei, M. The synthesis of imidazoles and evaluation of their antioxidant and antifungal activities. *Monatshefte Chem.* **149**, 1447–1452. https://doi.org/10.1007/s00706-020-02636-6 (2018).
10. Yardımcı, B. K. Imidazole antifungals: A review of their action mechanisms on cancerous cells. *Int. J. Second. Metabo.* **7**, 139–159. https://doi.org/10.21448/ijsm.714310 (2020).
11. Malhotra, V., Pathak, S. R., Nath, R., Mukherjee, D. & Shanker, K. Substituted imidazole derivatives as novel cardiovascular agents. *Bioorg. Med. Chem. Lett.* **21**, 936–939. https://doi.org/10.1016/j.bmcl.2010.12.029 (2011).
12. Navarrete-Vázquez, G. et al. Synthesis, vasorelaxant activity and antihypertensive effect of Benzo[d]imidazole derivatives. *Bioorg. Med. Chem.* **18**, 3985–3991. https://doi.org/10.1016/j.bmc.2010.04.038 (2010).
13. Unnisa, A. et al. Design, in Silico study, synthesis and in vitro evaluation of some N5-(1H-pyrazol-3-yl)-3H-benzo[d]imidazole-2,5-diamine derivatives as potential pancreatic lipase inhibitors for anti-obesity activity. *Eur. Rev. Med. Pharmacol. Sci.* **26**, 7245–7255. https://doi.org/10.26355/eurrev_202210_29917 (2022).
14. Chopra, P. N. & Sahu, J. K. Biological significance of Imidazole-based analogues in new drug development. *Current Drug Discov. Technol.* **17**, 574–584 https://doi.org/10.2174/1570163816666190320123340 (2020).
15. Kumar, N. & Goel, N. Recent development of imidazole derivatives as potential anticancer agents. *Phys. Sci. Rev.* **8**, 2903–2941. https://doi.org/10.1515/psr-2021-0041 (2023).
16. Murtazaeva, Z. et al. Imidazole hybrids: A privileged class of heterocycles in medicinal chemistry with new insights into anticancer activity. *Molecules* **30**, 2245. https://doi.org/10.3390/molecules30102245 (2025).
17. Sharma, D. et al. Synthesis, antimicrobial and antiviral evaluation of substituted imidazole derivatives. *Eur. J. Med. Chem.* **44**, 2347–2353. https://doi.org/10.1016/j.ejmech.2008.05.002 (2009).
18. Teli, P., Sahiba, N., Sethiya, A., Soni, J. & Agarwal, S. Imidazole derivatives: impact and prospects in antiviral drug discovery. *Imidazole-Based Drug Discov*. 167–193. https://doi.org/10.1016/B978-0-323-85479-5.00001-0 (2022).
19. Blanco, M. G. et al. Diisopropylphenyl imidazole (DII): A new compound that exerts anthelmintic activity through novel molecular mechanisms. *PLoS Negl. Trop. Dis.* **12**, e0007021. https://doi.org/10.1371/journal.pntd.0007021 (2018).
20. Bhatnagar, A., Sharma, P. K. & Kumar, N. A review on 'imidazoles': their chemistry and pharmacological potentials. *Int. J. PharmTech Res.* **3**, 268–282 (2011).
21. Pandey, J. et al. Synthesis and antitubercular screening of imidazole derivatives. *Eur. J. Med. Chem.* **44**, 3350–3355. https://doi.org/10.1016/j.ejmech.2009.02.013 (2009).
22. Parwani, D. et al. Current insights into the chemistry and antitubercular potential of benzimidazole and imidazole derivatives. *Mini-Rev. Med. Chem.* **21**, 643–657. https://doi.org/10.2174/1389557520666201102094401 (2021).
23. de Lócio, L. L. et al. Application of heterocycles as an alternative for the discovery of new Anti-ulcer compounds: A mini-review. *Curr. Pharm. Design*. **28**, 1373–1388. https://doi.org/10.2174/1381612828666220512095559 (2022).
24. Shah, J. S. & Patel, J. R. Anti-ulcer activity of lucer against experimentally induced gastric ulcers in rats. *Ayu* **33**, 314–316. https://doi.org/10.4103/0974-8520.105260 (2012).
25. Singh, D., Kharb, R. & Sharma, S. K. Schiff's base imidazole derivatives synthesis and evaluation for their Anti-Inflammatory activity. *Orient. J. Chem.* **40**, 152–164. https://doi.org/10.13005/ojc/400119 (2024).
26. Krishna, G. A. et al. Transition metal complexes of imidazole derived schiff bases: Antioxidant/anti inflammatory/antimicrobial/enzyme inhibition and cytotoxicity properties. *J. Mol. Struct.* https://doi.org/10.1016/j.molstruc.2022.134384 (2023).
27. Goel, K. K. et al. Imidazoles as serotonin receptor modulators for treatment of depression: Structural insights and structure–activity relationship studies. *Pharmaceutics* 15, 2208 : (2023). https://doi.org/10.3390/pharmaceutics15092208
28. Abramets, I. I., Zayka, T. O., Evdokimov, D. V. & Kuznetsov, Y. V. ir Y. V. Sidorova. Researches of the imidazole and indole derivatives cerebroprotective activity and its impact on effects of antidepressants. *Фармакокинетика и фармакодинамика* **3**, 18–24. https://doi.org/10.37489/2587-7836-2020-1-18-24 (2020).

29. Sadula, A. & Gaddhe, L. Synthesis, computational studies and biological evaluation of novel Acenaphthoquinone-imidazole derivatives as dual inhibitors of HSP90 and Topo II in cancer therapy. *Results Chem.* **5**, 100796. https://doi.org/10.1016/j.rechem.2023.100796 (2023).
30. Hamad, H. T. The anti-cancer effectiveness of some heterocyclic compounds containing sulfur atom. *Results Chem.* **15**, 102182. https://doi.org/10.1016/j.rechem.2025.102182 (2025).
31. Vainauskas, V. et al. Synthesis and characterization of Sulfonamide-Imidazole hybrids with in vitro antiproliferative activity against Anthracycline-Sensitive and resistant H69 small cell lung cancer cells. *ChemMedChem* **20** (e202500260). https://doi.org/10.1002/cmdc.202500260 (2025).
32. Balandis, B. et al. Synthesis of novel Benzenesulfonamide-Bearing functionalized imidazole derivatives as novel candidates targeting Multidrug-Resistant Mycobacterium abscessus complex. *Microorganisms* **11**, 935. https://doi.org/10.3390/microorganisms11040935 (2023).
33. Han, S., Mei, L., Quach, T., Porter, C. & Trevaskis, N. Lipophilic conjugates of drugs: A tool to improve drug Pharmacokinetic and therapeutic profiles. *Pharmacol. Res.* **38**, 1497–1518. https://doi.org/10.1007/s11095-021-03093-x (2021).
34. Marinković, J. et al. Silver(I) complexes bearing S-Alkyl Thiosalicylic acid derivatives: DNA/BSA binding and antitumor activity in vitro and in vivo. *Pharmaceutics* **17**, 1340. https://doi.org/10.3390/pharmaceutics17101340 (2025).
35. Yang, Y., Engkvist, O., Llinàs, A. & Chen, H. Beyond size, ionization state, and lipophilicity: influence of molecular topology on absorption, distribution, metabolism, excretion, and toxicity for druglike compounds. *J. Med. Chem.* **55**, 3667–3677. https://doi.org/10.1021/jm201548z (2012).
36. Karthik, V., Bhat, I. A. & Anantharaman, G. Backbone thio-functionalized Imidazol-2-ylidene–Metal complexes: Synthesis, structure, electronic properties, and catalytic activity. *Organometallics* **32**, 7006–7013. https://doi.org/10.1021/om400585b (2013).
37. Yurttaş, L., Duran, M., Demirayak, Ş., Gençer, H. K. & Tunalı, Y. Synthesis and initial biological evaluation of substituted 1-phenylamino-2-thio-4,5-dimethyl-1*H*-imidazole derivatives. *Bioorg. Med. Chem. Lett.* **23**, 6764–6768. https://doi.org/10.1016/j.bmcl.2013.10.024 (2013).
38. Joshi, V. M. et al. Practical and efficient synthesis of 2-Thio-imidazole Derivative—ZY12201: A potent TGR5 agonist. *Org. Process Res. Dev.* **24**, 1508–1514. https://doi.org/10.1021/acs.oprd.0c00234 (2020).
39. Karakaya, A., Çevik, U. A., Erçetin, T., Özkay, Y. & Kaplancıklı, Z. A. Synthesis of Imidazole-Thiazole derivatives as acetylcholinesterase and butyrylcholinesterase inhibitory activities. *Pharm. Chem. J.* **57**, 1439–1443 (2023).
40. Lange, J. H. M. et al. Probing the cannabinoid CB1/CB2 receptor subtype selectivity limits of 1,2-diarylimidazole-4-carboxamides by fine-tuning their 5-substitution pattern. *Bioorg. Med. Chem. Lett.* **20**, 2770–2775. https://doi.org/10.1016/j.bmcl.2010.03.068 (2010).
41. Yang, J., Zeng, T., Yan, K., Qin, Z. & Wen, J. Direct synthesis of alkylthioimidazoles: One-pot three-component cross-coupling mediated by paired electrolysis. *Adv. Synth. Catal.* https://doi.org/10.1002/adsc.202200259 (2022).
42. Langarizadeh, M. A., Ameri, A., Tavakoli, M. R., Abiri, A. & Forootanfar, H. The Trimethoxyphenyl (TMP) functional group: a versatile pharmacophore. *Med. Chem. Res.* **32**, 2473–2500. https://doi.org/10.1007/s00044-023-03153-4 (2023).
43. Ghawanmeh, A. A., Al-Bajalan, H. M., Mackeen, M. M., Alali, F. Q. & Chong, K. F. Recent developments on (-)-colchicine derivatives: synthesis and structure-activity relationship. *Eur. J. Med. Chem.* **185**, 111788. https://doi.org/10.1016/j.ejmech.2019.111788 (2020).
44. Imbert, T. F. Discovery of podophyllotoxins. *Biochimie* **80**, 207–222. https://doi.org/10.1016/s0300-9084(98)80004-7 (1998).
45. Tang, S., Zhou, Z., Jiang, Z., Zhu, W. & Qiao, D. Indole-Based tubulin inhibitors: Binding modes and SARs investigations. *Molecules* **27**, 1587. https://doi.org/10.3390/molecules27051587 (2022).
46. Ravelli, R. B. G. et al. Insight into tubulin regulation from a complex with Colchicine and a stathmin-like domain. *Nature* **428**, 198–202. https://doi.org/10.1038/nature02393 (2004).
47. Semenov, V. V. et al. Synthesis of antimitotic polyalkoxyphenyl derivatives of combretastatin using plant Allylpolyalkoxybenzenes. *J. Nat. Prod.* **73**, 1796–1802. https://doi.org/10.1021/np1004278 (2010).
48. Wang, Q. et al. Structural modification of the 3,4,5-Trimethoxyphenyl moiety in the tubulin inhibitor VERU-111 leads to improved antiproliferative activities. *J. Med. Chem.* **61**, 7877–7891. https://doi.org/10.1021/acs.jmedchem.8b00827 (2018).
49. Jędrzejczyk, M. et al. Novel combretastatin A-4 Analogs—Design, Synthesis, and antiproliferative and Anti-Tubulin activity. *Molecules* **29**, 2200. https://doi.org/10.3390/molecules29102200 (2024).
50. Grisham, R., Ky, B., Tewari, K. S., Chaplin, D. J. & Walker, J. Clinical trial experience with CA4P anticancer therapy: Focus on efficacy, cardiovascular adverse events, and hypertension management. *Gynecol. Oncol. Res. Pract.* **5**, 1. https://doi.org/10.1186/s40661-017-0058-5 (2018).
51. Jeong, C. H., Park, H. B., Jang, W. J., Jung, S. H. & Seo, Y. H. Discovery of hybrid Hsp90 inhibitors and their anti-neoplastic effects against gefitinib-resistant non-small cell lung cancer (NSCLC). *Bioorg. Med. Chem. Lett.* **24**, 224–227. https://doi.org/10.1016/j.bmcl.2013.11.034 (2014).
52. Li, Y. et al. Hexamethoxylated monocarbonyl analogues of Curcumin cause G2/M cell cycle arrest in NCI-H460 cells via Michael Acceptor-Dependent redox intervention. *J. Agric. Food Chem.* **63**, 7731–7742. https://doi.org/10.1021/acs.jafc.5b02011 (2015).
53. Ma, L. Y. et al. Design, Synthesis, and Structure–Activity relationship of novel LSD1 inhibitors based on Pyrimidine–Thiourea hybrids as Potent, orally active antitumor agents. *J. Med. Chem.* **58**, 1705–1716. https://doi.org/10.1021/acs.jmedchem.5b00037 (2015).
54. Mohedas, A. H. et al. Structure-activity relationship of 3,5-diaryl-2-aminopyridine ALK2 inhibitors reveals unaltered binding affinity for fibrodysplasia ossificans progressiva causing mutants. *J. Med. Chem.* **57**, 7900–7915. https://doi.org/10.1021/jm501177w (2014).
55. Singh, S. et al. Design and synthesis of human ABCB1 (P-glycoprotein) inhibitors by peptide coupling of diverse chemical scaffolds on carboxyl and amino termini of (S)-valine-derived thiazole amino acid. *J. Med. Chem.* **57**, 4058–4072. https://doi.org/10.1021/jm401966m (2014).
56. Belani, C. P., Doyle, L. A. & Aisner, J. Etoposide: Current status and future perspectives in the management of malignant neoplasms. *Cancer Chemother. Pharmacol.* **34**, 118–126. https://doi.org/10.1007/BF00684875 (1994). Suppl.
57. Clark, P. I. & Slevin, M. L. The clinical Pharmacology of Etoposide and Teniposide. *Clin. Pharmacokinet.* **12**, 223–252. https://doi.org/10.2165/00003088-198712040-00001 (1987).
58. Alvarado-Luna, G. & Morales-Espinosa, D. Treatment for small cell lung cancer, where are we now?—a review. *Transl. Lung Cancer Res.* **5**, 26–38. https://doi.org/10.3978/j.issn.2218-6751.2016.01.13 (2016).
59. O'Dwyer, P. J. et al. Trimetrexate: Clinical development of a nonclassical antifolate. *NCI Monogr.* 105–109 (1987).
60. Zheng, C. H. et al. Synthesis and biological evaluation of 1-Phenyl-1,2,3,4-dihydroisoquinoline compounds as tubulin polymerization inhibitors. *Arch. Pharm.* **345**, 454–462. https://doi.org/10.1002/ardp.201100169 (2012).
61. Zurlo, M. et al. Synergistic effects of a combined treatment of glioblastoma U251 cells with an anti-miR-10b-5p molecule and an antiCancer agent based on 1-(3′,4′,5′-Trimethoxyphenyl)-2-Aryl-1H-Imidazole scaffold. *Int. J. Mol. Sci.* **23**, 5991. https://doi.org/10.3390/ijms23115991 (2022).
62. Liu, R. et al. Design, synthesis and bioevaluation of 6-aryl-1-(3,4,5-trimethoxyphenyl)-1*H*-benzo[*d*]imidazoles as tubulin polymerization inhibitors. *Eur. J. Med. Chem.* **226**, 113826. https://doi.org/10.1016/j.ejmech.2021.113826 (2021).
63. Meshram, G. A. & Vala, V. A. Synthesis, characterization, and antimicrobial activity of benzimidazole-derived Chalcones containing 1,3,4-oxadiazole moiety. *Chem. Heterocycl. Compd.* **51**, 44–50 (2015).
64. Zhao, D. G. et al. Synthesis and structure–activity relationships of N-methyl-5,6,7-trimethoxylindoles as novel antimitotic and vascular disrupting agents. *J. Med. Chem.* **56**, 1467–1477. https://doi.org/10.1021/jm3014663 (2013).

65. Metwally, K. et al. Structure–activity relationship investigation of methoxy substitution on anticancer pyrimido[4,5-c]quinolin-1(2H)-ones. *Med. Chem. Res.* **22**, 4481–4491. https://doi.org/10.1007/s00044-012-0428-9 (2013).
66. Elejalde-Cadena, N. R., García-Olave, M., Macías, M. A. & Portilla, J. Influence of halogen atoms and hydrogen bonds in the crystal structure of 1,2,4-trisubstituted imidazoles having haloaryl groups. *J. Mol. Struct.* **1286**, 135662. https://doi.org/10.1016/j.molstruc.2023.135662 (2023).
67. Mattiello, L., Rehim, S. S. A., Manic, G., & Vitale, I. Assessment of cell cycle progression and mitotic slippage by videomicroscopy. In *Methods Cell Biology,* Vol. 181 43–58 (Academic Press, 2024). https://doi.org/10.1016/bs.mcb.2023.03.004
68. Lu, C. et al. Cell apoptosis: requirement of H2AX in DNA ladder formation but not for the activation of Caspase-3. *Mol. Cell.* **23**, 121–132. https://doi.org/10.1016/j.molcel.2006.05.023 (2006).
69. Podhorecka, M., Skladanowski, A. & Bozko, P. H. A. X. Phosphorylation its role in DNA damage response and cancer therapy. *J. Nucleic Acids*. https://doi.org/10.4061/2010/920161 (2010).
70. Bakhoum, S. F., Kabeche, L., Compton, D. A., Powell, S. N. & Bastians, H. Mitotic DNA damage response: At the crossroads of structural and numerical cancer chromosome instabilities. *Trends Cancer*. **3**, 225–234. https://doi.org/10.1016/j.trecan.2017.02.001 (2017).
71. Georgoulis, A., Vorgias, C. E., Chrousos, G. P. & Rogakou, E. P. Genome instability and γH2AX. *Int. J. Mol. Sci.* **18**, 1979. https://doi.org/10.3390/ijms18091979 (2017).
72. Elmore, S. Apoptosis: A review of programmed cell death. *Toxicol. Pathol.* **35**, 495–516. https://doi.org/10.1080/01926230701320337 (2007).
73. Shah, S. & D'Souza, G. G. M. Modeling tumor microenvironment complexity in vitro: spheroids as physiologically relevant tumor models and strategies for their analysis. *Cells* **14**, 732. https://doi.org/10.3390/cells14100732 (2025).
74. Cheng, B. & Crasta, K. Consequences of mitotic slippage for antimicrotubule drug therapy. *Endocr. Relat. Cancer*. **24**, T97–T106. https://doi.org/10.1530/ERC-17-0147 (2017).
75. Sinha, D., Duijf, P. H. G. & Khanna, K. K. Mitotic slippage: An old Tale with a new twist. *Cell. Cycle*. **18**, 7–15. https://doi.org/10.1080/15384101.2018.1559557 (2019).
76. Daina, A., Michielin, O. & Zoete, V. SwissADME: A free web tool to evaluate pharmacokinetics, drug-likeness and medicinal chemistry friendliness of small molecules. *Sci. Rep.* **7**, 42717. https://doi.org/10.1038/srep42717 (2017).
77. Waring, M. J. et al. An analysis of the attrition of drug candidates from four major pharmaceutical companies. *Nat. Rev. Drug Discov.* **14**, 475–486. https://doi.org/10.1038/nrd4609 (2015).
78. Lipinski, C. A. Lead- and drug-like compounds: the rule-of-five revolution. *Drug Discov. Today: Technol.* **1**, 337–341. https://doi.org/10.1016/j.ddtec.2004.11.007 (2004).
79. Veber, D. F. et al. Molecular properties that influence the oral bioavailability of drug candidates. *J. Med. Chem.* **45**, 2615–2623. https://doi.org/10.1021/jm020017n (2002).
80. Doak, B. C., Over, B., Giordanetto, F. & Kihlberg, J. Oral druggable space beyond the rule of 5: Insights from drugs and clinical candidates. *Chem. Biol.* **21**, 1115–1142. https://doi.org/10.1016/j.chembiol.2014.08.013 (2014).
81. Buchwald, P. *Drug-Like Properties Concepts, Structure Design and Methods from ADME To Toxicity Optimization* (Academic, 2016).
82. Pranaitytė, G. et al. Exploration of 1-(2,4-difluorophenyl)-5-oxopyrrolidine-3-carboxylic acid derivatives effect on triple-negative breast, prostate cancer and melanoma cell 2D and 3D cultures. *Sci. Rep.* **15**, 17590. https://doi.org/10.1038/s41598-025-02106-8 (2025).

Author contributions

N.M., B.G., K.A. and V.M. conceived the study and curated the data. Funding was acquired by N.M. and V.M. Formal analysis was performed by N.M. and B.G. Methodology was developed by B.G. Project administration was carried out by N.M. and V.M. Resources were provided by N.M. Figures and visualizations were prepared by B.G. and N.M. Validation was conducted by N.M., B.G., K.A. and V.M. The original manuscript draft was written by N.M., V.M. and B.G. All authors reviewed and edited the final version of the manuscript.

Declarations

Competing interests

The authors declare no competing interests.

Additional information

Supplementary Information The online version contains supplementary material available at https://doi.org/10.1038/s41598-026-36890-8.

Correspondence and requests for materials should be addressed to N.M. or B.G.

Reprints and permissions information is available at www.nature.com/reprints.

Publisher's note Springer Nature remains neutral with regard to jurisdictional claims in published maps and institutional affiliations.